2006

The interplay between star formation and the nuclear environment of our Galaxy: deep X-ray observations of the Galactic centre Arches and Quintuplet clusters

QD Wang
University of Massachusetts - Amherst

H Dong

C Lang

Recommended Citation

Wang, QD; Dong, H; and Lang, C, "The interplay between star formation and the nuclear environment of our Galaxy: deep X-ray observations of the Galactic centre Arches and Quintuplet clusters" (2006). *Monthly Notices of the Royal Astronomical Society*. 1087.
https://doi.org/10.1111/j.1365-2966.2006.10656.x

The Interplay between Star Formation and the Nuclear Environment of our Galaxy: Deep X-ray Observations of the Galactic Center Arches and Quintuplet Clusters

Q. Daniel Wang[1], Hui Dong[1], & Cornelia Lang[2]

ABSTRACT

The Galactic center (GC) provides a unique laboratory for a detailed examination of the interplay between massive star formation and the nuclear environment of our Galaxy. Here, we present an 100 ks *Chandra* ACIS observation of the Arches and Quintuplet star clusters. We also report on a complementary mapping of the dense molecular gas near the Arches cluster made with the Owens Valley Millimeter Array. We present a catalog of 244 point-like X-ray sources detected in the observation. Their number-flux relation indicates an over-population of relatively bright X-ray sources, which are apparently associated with the clusters. The sources in the core of the Arches and Quintuplet clusters are most likely extreme colliding wind massive star binaries. The diffuse X-ray emission from the core of the Arches cluster has a spectrum showing a 6.7-keV emission line and a surface intensity profile declining steeply with radius, indicating an origin in a cluster wind. In the outer regions near the Arches cluster, the overall diffuse X-ray enhancement demonstrates a bow shock morphology and is prominent in the Fe Kα 6.4-keV line emission with an equivalent width of ~ 1.4 keV. Much of this enhancement may result from an ongoing collision between the cluster and the adjacent molecular cloud, which have a relative velocity $\gtrsim 120$ km^{-1}. The older and less compact Quintuplet cluster contains much weaker X-ray sources and diffuse emission, probably originating from low-mass stellar objects as well as a cluster wind. However, the overall population of these objects, constrained by the observed *total* diffuse X-ray luminosities, is substantially smaller than expected for both clusters, if they have normal Miller & Scalo initial mass functions. This deficiency of low-mass objects may be a manifestation of the unique star formation environment of the Galactic center, where high-velocity cloud-cloud and cloud-cluster collisions are frequent.

Subject headings: Galaxy: center, individual (Arches, Quintuplet) — X-rays: ISM — stars: formation, Wolf-Rayet, winds, outflows — ISM: clouds

1. Introduction

Nuclear regions of galaxies are the breeding ground of high energy phenomena and processes, which are manifested observationally by active galactic nuclei (AGNs) and star-bursts. Such activities are believed to be important in both regulating galaxy evolution and generating thermal and chemical feedback into the intergalactic medium. The best site for a detailed study of the activities and their complex interaction with the physically extreme environment in the nuclear regions of galaxies is our own nucleus, only ~ 8 kpc away. We can observe the Galactic center (GC) with a spatial resolution and sensitivity that are factors $\gtrsim 300$ and $\gtrsim 10^5$ better than those available for even nearby nuclear starburst galaxies (e.g., M82 and NGC 253) or AGNs (e.g., M81).

While the super-massive black hole at the dynamic center of the Galaxy is only weakly active at present (Baganoff et al. 2001), much of the cur-

[1]Department of Astronomy, B619E-LGRT, University of Massachusetts, Amherst, MA 01003; wqd@astro.umass.edu, hdong@astro.umass.edu

[2]Department of Physics and Astronomy, University of Iowa, Iowa City, IA 52245; cornelia-lang@uiowa.edu

rent high-energy activity in the GC is due to the presence of the three young massive stellar clusters in the central 50 pc: Arches (with age equal to $2-3\times10^6$ yrs; core or half-mass radius 0.4 pc), Quintuplet ($3-6\times10^6$ yrs; 1.0 pc), and the Central cluster ($3-7\times10^6$ yrs; 0.5 pc) (Figer et al. 1999, 2002, 2004; Stolte et al. 2002; Genzel et al. 2003). These clusters are responsible for about half of the Lyman continuum flux emitted in the central several 10^2 pc of the GC. Massive stars are also expected to release large amounts of mechanical energy into the GC region in form of fast stellar winds and supernovae, although the actual rate is highly uncertain. This mechanical energy input shapes the surrounding ISM. The present work focuses on the Arches and Quintuplet clusters. The GC cluster is less massive and older. Its location in the circum-nuclear region makes its X-ray properties difficult to characterize and will not be dealt with here (however see Nayakshin et al. 2005).

Both the Arches and Quintuplet clusters are known X-ray emitters. Discovered serendipitously at a large off-axis angle ($\sim 7'$) in an initial 50 ks *Chandra* ACIS-I observation (Yusef-Zadeh et al. 2002), the X-ray emission arising from the Arches cluster was resolved into discrete and diffuse components. In a later 12 ks ACIS-I observation during a large-scale GC survey (Wang et al. 2002a), the X-ray core of the cluster was further resolved into two separate components (Wang 2003; Law & Yusef-Zadeh 2004). The apparent diffuse X-ray component was speculated to arise from the so-called cluster wind (Raga et al. 2001; Yusef-Zadeh et al. 2002). Because of the high number density of massive stars, their stellar winds collide with each other and can be largely thermalized to form a plasma with an initial temperature of a few times 10^7 K. The expanding of this plasma may then be considered as a wind from the entire cluster. However, the quality of the previous observations is not adequate for a quantitative test of this scenario. In particular, the diffuse X-ray spectrum shows a distinct 6.4-keV emission line from neutral or weakly ionized irons. The origin of this line is unknown. The X-ray emission from the Quintuplet cluster is substantially weaker. The detection of a few discrete sources and possible diffuse emission in the region has been reported; but detailed spectral and timing information is not yet available (Wang 2003; Law & Yusef-Zadeh 2004)

To further the study of these two clusters and their relationship to the environment, we have obtained an 100 ks *Chandra* ACIS-I observation. We have further carried out a complementary imaging study of the molecular gas in the immediate surroundings of the Arches cluster using the six-element Owens Valley Millimeter Array. With these observations and other multi-wavelength data, we present an in-depth study of various point-like and diffuse X-ray sources in and around the clusters.

In this paper, we assume that the distance to the GC is 8 kpc (hence $1' = 2.5$ pc) and quote statistical errors from our X-ray data analysis at the 90% confidence level, unless being pointed out otherwise. The solar abundance is in reference to Anders & Grevesse (1989); thus the number of iron relative to hydrogen is 4.68×10^{-5}, which is considerably greater than 2.69×10^{-5} in the so-called ISM abundance (Wilms & McCray 2002), for example.

2. Observations and Data Reduction

2.1. *Chandra* Observations

Our deep *Chandra* ACIS-I observation (Obs. ID: 4500) was carried out on June 9, 2004. The Arches cluster was placed about $1'$ away from the aim-point to minimize the effect of the CCD gaps on mapping the extended X-ray emission around the cluster. This slight offset from the axis had a negligible effect on the spatial resolution for the Arches cluster. We used the "very faint" mode for a better discrimination and removal of charged particle induced events. We have reprocessed the data, using the CIAO software (version 3.2.1) and calibration database (version 3.0.0). This reprocessing includes both charge transfer inefficiency (CTI) and gain corrections as well as the removal of time intervals contaminated by background flares. The total reprocessed good time (live-time) is 98.6 ks. We create ACIS-I event images and corresponding exposure maps in the 1-2.5, 2.5-4, 4-6, and 6-9 keV bands.

We detect X-ray sources, following the same procedure as detailed in Wang (2004). The detection, optimized for point-like sources, uses a combination of algorithms: wavelet, sliding-box, and maximum likelihood centroid fitting. The source detections are carried out in the 1-4 keV, 4-9 keV,

and 1-9 keV bands. The detected sources in the three bands are merged together. Multiple detections with overlapping 2σ centroid error circles are considered to be the same source, and the centroid with the smallest error is adopted. The accepted source candidates generally have individual local false detection probabilities $P \leq 10^{-7}$. But in the vicinity ($2' \times 2'$ field) of the clusters, we also include sources detected with reduced significances $10^{-7} < P \leq 10^{-5}$. Over the entire search, the expected false detection probability is ~ 1.

We check the astrometry of the X-ray observation, based on the multi-wavelength comparisons. A SIMBAD search gives some potential counterparts within the 3σ error radius around each detected X-ray source. A few sources in the Arches cluster have radio counterparts, which have accurate positions ($\sim 0\farcs1$; Lang et al. 2005. A comparison of the two bright X-ray/radio pairs (92/AR1 and 93/AR4; Table 2) shows that their positions are all within $0\farcs3$, consistent with their statistical and systematic uncertainties (Table 1). Finding exact matches of X-ray sources with near-IR objects is generally more difficult, because they are numerous and typically have relatively large absolute position uncertainties of $\sim 1'' - 2''$. We approximately correct for the relatively shifts of the near-IR positions to the X-ray positions, using the original *HST* NICMOS observations of the Arches and Quintuplet clusters as well as the coordinates of individual NIR objects (2, 6, 7, and 9 for the Arches and 211, 242, 231, and 257 for the Quintuplet) listed in (Figer et al. 1999a; Figer et al. 2002). The *HST*-to-*Chandra* RA. and Dec. shifts are -$0\farcs52$ and $0\farcs29$ for the Arches cluster and -$0\farcs43$ and -$0\farcs32$ for the Quintuplet cluster, respectively. These shifts are then applied to the NICMOS images to facilitate the comparison with the X-ray data. The uncertainties in these astrometry corrections should be around $0\farcs3$, dominated by the errors in the X-ray source centroids.

To construct "diffuse" X-ray maps, we excise the detected sources from the ACIS-I data. For each source with a count rate (CR) $\leq$ 0.01 counts s^{-1}, we exclude a circular region with a radius of 1.5 times the 90% PSF energy enclosed radius (EER). For sources with CR > 0.01 cts/s, this radius is multiplied by an additional factor of 1+log(CR/0.01) to further minimize the contamination from the PSF wing.

For the background subtraction in our imaging analysis, we use the blank-sky data with a total exposure of 550 ks. The data are re-projected to mimic individual observations. The background subtraction is mostly to remove the contribution from events induced by charged particles. Of course, the blank-sky data also contains cosmic X-ray radiation. Its intensity varies from one part of the sky to another, mostly at energies below ~ 1 keV. At higher energies, the radiation is negligible, compared to the fluxes due to charged particle-induced events and to the emission from the GC region. The combination of the background subtraction and the exposure correction then gives the flat-fielded intensity images in individual bands.

In addition to the broad-band images, we also construct narrow-band images of the prominent 6.4-keV and 6.7-keV emission lines in the energy ranges of 6.25-6.55 keV and 6.55-7 keV. Because the counting statistics at energies greater than 7 keV is too poor, we estimate the continuum contribution to these narrow bands, based on the intensities measured in the 4-5 keV and 5-6.2 keV bands. We assume an intrinsic power law spectral shape of the blank-sky background-subtracted diffuse emission in the 4-7 keV range and account for both the effective area and energy response of the instrument, using the convolved model outputs from the X-ray spectral analysis software XSPEC. The continuum-subtracted line intensity image, divided by the specific continuum intensity, gives the equivalent width (EW) map of the line. The calculation at each image pixel is carried out adaptively, using a Gaussian kernel with its size adjusted to achieve a signal-to-noise ratio greater than five at each step.

We further include all available archival ACIS-I observations that were taken before our deep observation and covered the clusters (Yusef-Zadeh et al. 2002; Wang et al. 2002a) in analyzes that do not require the maximum spatial resolution offered by our on-axis observation. The combined data have an effective exposure of 157 ks at Arches and 160 ks at Quintuplet. Source detections are also carried out for these individual observations and are used to examine the potential long-term variability of the sources in the close vicinity of the clusters. For detailed spatial and spectral analyzes of the Arches cluster, we use only our on-axis deep *Chandra* observation. But for the Quintuplet clus-

ter, all the observations are off-axis and and are thus used. Because the effective area and spectral response depend on both time and position, we extract spectra from individual observations separately and then combine them together using the FTOOLS routine "addspec", which produces weighted effective area and spectral response files. All spectral extractions use the "Gaussian error", not the "Poisson error", which is the default of the CIAO *psextract* routine and actually uses the Gehrels's approximation (Gehrels 1986). This latter method could cause problems in the error propagation through the spectral co-adding. For bright X-ray point-like sources in the Arches cluster, we typically group such spectra to achieve a minimum 20 counts per bin. For diffuse X-ray emission spectra, the noise contribution from the subtracted background becomes important. We group the spectra to have the *background-subtracted* signal-to-noise (S/N) in each bin greater than 3 for the Arches cluster and 2 for the Quintuplet cluster with fainter diffuse X-ray emission.

2.2. CS (J=2-1) Molecular Line Observations

The region around the GC Radio Arc (where the Quintuplet and Arches clusters are located) harbors a number of large, dense molecular clouds. The so-called "-30 km s^{-1} cloud" is believed to be ionized by the Arches cluster (Lang et al 2001a, 2002). High resolution ($\sim 10''$) observations of part of this cloud complex which immediately surrounds the Arches cluster were made in the 3.4 mm continuum and CS (J=2-1) line using the six-element millimeter array at the Owens Valley Radio Observatory (OVRO) in March, April, May and June 2002. Two telescope configurations (equatorial and low) were used, with baselines ranging from 15 to 100 m. Six fields with a primary beam of $60''$ were observed in a mosaic pattern, with a spacing of $30''$. The resulting mosaic covers an area of approximately $4' \times 3'$ centered on the position $RA = 17^h46^m51^s, DEC = -28°49'00''$ (J2000). The total integration time on each of the six fields was approximately 4 hours.

NRAO 530, 3C 273, and Neptune were used for gain, passband, and absolute flux calibration, respectively. The data were calibrated using the MMA package (Scoville et al. 1993), and the mosaicking was carried out with the maximum entropy method of de-convolution implemented in the MIRIAD routine MOSMEM (Cornwell & Braun 1988; Sault, Staveley-Smith, & Brouw 1996). The CS (J=2-1) line data were taken at a rest frequency of 97.981 GHz, with 64 channels of 0.5 MHz width, corresponding to a velocity resolution of 1.53 km s^{-1} and a total velocity coverage of 96 km s^{-1}. The line was centered on $v_{LSR} = -20$ km s^{-1}. Simultaneous 3.4 mm continuum observations were made with a bandwidth of 1 GHz.

The largest spatial scale to which the OVRO interferometer is sensitive is $20''$, corresponding to the shortest baseline of 15 m at 3.4 mm. Therefore, more extended structures are not detected. In order to recover the missing flux density, the total power measurements from single-dish observations of this region have been added. Single-dish observations of the CS (2-1) line in the -30 km s^{-1} molecular cloud were carried out with the *IRAM* 30 m telescope by (Serabyn & Gusten 1987). Spectra in the vicinity of the Arched Filaments complex were obtained at regular grid spacings of $18''$ and imaged with a single-dish beam size of $25''$. These observations were centered at $v_{LSR} = 0$ km s^{-1}, using a 512-channel filter bank with 1 MHz resolution, which corresponds to a velocity resolution of 3.06 km s^{-1}.

Since there is reasonable overlap between the shortest spacings of the OVRO interferometer (4 kilo-lambda) and the diameter of the 30 m antenna (8 kilo-lambda), the linear technique of "feathering" single-dish and interferometer data is appropriate. This method requires that the single-dish data be a good representation of the object at low spatial frequencies, and that the interferometer mosaic be a good representation at mid-to-high spatial frequencies. The feathering technique can be carried out using the MIRIAD task IMMERGE. We input de-convolved and restored single-dish and interferometric images with the same velocity resolution and spatial grid. IMMERGE first transforms the images into the Fourier plane, where the data are combined. In the case of the 30 m single dish data and OVRO millimeter array data, the flux densities in the overlap region (4-8 kilolambda) agree at the 10% level. The single-dish data are given unit weight, and the low spatial frequencies of the interferometer data are adjusted in the Fourier plane with a

taper such that a combination of the single-dish and interferometer data results in an image with a Gaussian beam equal in diameter to the beam of the input interferometer mosaic image ($\sim 9'' \times 9''$).

3. Analysis and Results

The entire field of our deep ACIS-I observation is shown in Fig. 1, while Fig. 2 gives close-ups of the Arches and Quintuplet clusters. In this section, we first examine the overall X-ray source population in the field of the observation and then present a detailed characterization of discrete sources and diffuse emission in the Arches and Quintuplet regions, separately.

3.1. Discrete X-ray Sources

Table 1 summarizes the key parameters of our detected X-ray sources in the deep ACIS-I observation. The note to this table explains various parameters listed. The hardness ratios, in particular, provide simple source spectral characteristics, which may be compared with model predictions (e.g., Fig. 3). A few sources show exceptionally large HR2 values, which could be reproduced with the assumed models only with abnormal parameters (e.g., a power law with a photon index $\Gamma < 0$ or a plasma with an iron abundance $> 2\times$solar). Assuming a plasma with a higher temperature ($\gtrsim 6$ keV) would not help, which reduces the He-like Fe line emission and hence the HR2 value.

We check timing variability for each of the sources, based on a Kolmogorov-Smirnov test with the light curve of the source-removed background as a reference. The test is performed in all three source detection energy bands. Only Source #20 (J174532.27-285052.3) in the table shows marginal evidence (3σ) for variability.

The brightest source in the field is LMXB 1E 1743.1-2843 with an X-ray luminosity of $L_X \sim 2 \times 10^{36}$ ergs s^{-1} in the 2-10 keV band (assuming at the distance of the GC; Porquet et al. 2003). The second brightest source is apparently a renewed X-ray burst of XMMU J174554.4-285456 (Porquet et al. 2005), detected during an *XMM-Newton* observation performed on October 3, 2002. This source did *not* appear in a *Chandra* observation (OBSID #3549, June, 19, 2003) in-between the *XMM-Newton* observation and our detection here (June 9, 2004). The source was also present in the two subsequent *Chandra* observations (OBSID #4683, July 5, 2004 and #4684, July 6, 2004), but not in later ones (e.g., OBSID # 5360, August 28, 2004).

The X-ray sources in the close vicinities of the Arches and Quintuplet clusters are marked in Fig. 2. Those in the NICMOS fields are listed in Table 2, including apparent near-IR and radio counterparts, which most likely represent massive stars if at the distance of the GC. In particular, two of the three strongest X-ray sources in the Arches cluster have radio counterparts (AR1 and AR4; Lang et al. 2005). The faint and apparently resolved J174549.73-284926.1 is probably associated with a close pair of radio sources of AR6 and AR10 (Lang et al. 2005); AR6, in particular, has a unique nonthermal radio spectrum with a spectral index of -0.7, whereas other radio sources in the field all have positive indexes (Lang et al 2001b; Lang et al. 2005).

To characterize the X-ray source number-flux relation (NFR) in the region, we need to account for various complications involved in the source detection and the confusion with interlopers (foreground stars and background AGNs). For simplicity, our NFR analysis here uses only the sources best-detected in the B band and with $P \leq 10^{-7}$ (Table 1) and with count rates smaller than 2×10^{-2} counts s^{-1} (hence both LMXB 1E 1743.1-2843 and the transient XMMU J174554.4-285456 are excluded). This filtering, resulting in a sample of total 186 sources, minimizes the confusion with foreground stars (typically with soft X-ray spectra and relatively low sight-line absorptions) and background AGNs (hard spectra and high absorptions), which should be preferentially detected in either the 1-4 keV band (a total of 18 sources) or the 4-9 keV band (29 sources), respectively. Eleven of the 18 soft sources and nine of the 29 hard sources are also detected in the 1-9 keV band, though not preferentially. As will be shown in § 3.2 and § 3.3, the absorptions towards the Arches and Quintuplet are ~ 5 and 8×10^{22} cm^{-2}, sampling a reasonable range of the column density toward the GC over the ACIS-I field (Fig. 1). The average total column density through the entire Galactic disk in the field is thus likely to be $\sim (1-2) \times 10^{23}$ cm^{-2}.

The source detection completeness varies across

TABLE 1
Chandra SOURCE LIST

Source (1)	CXGCS Name (2)	δ_x ($''$) (3)	CR (cts ks^{-1}) (4)	HR (5)	HR2 (6)	Flag (7)
85	J174549.73-284926.1	0.3	0.43 ± 0.08	–	–	B, H
90	J174550.26-284911.9	0.2	7.48 ± 0.29	-0.32 ± 0.05	-0.30 ± 0.06	B, S, H
92	J174550.41-284922.4	0.2	11.03 ± 0.36	-0.34 ± 0.04	-0.40 ± 0.05	B, S, H
93	J174550.47-284919.7	0.2	6.90 ± 0.29	-0.39 ± 0.05	-0.50 ± 0.06	B, S, H
213	J174614.44-284908.6	0.6	1.49 ± 0.14	0.27 ± 0.12	-0.65 ± 0.09	B, H, S
214	J174614.51-284937.2	0.6	0.70 ± 0.11	-0.81 ± 0.12	–	B, S
215	J174614.67-284940.3	0.7	0.34 ± 0.09	–	–	B, S
216	J174615.14-284932.9	0.7	0.50 ± 0.10	–	–	B, S
217	J174615.85-284945.5	0.8	0.57 ± 0.10	–	–	B, H
219	J174616.29-284940.8	0.8	0.34 ± 0.09	–	–	B, H
Sources detected with $10^{-7} < P < 10^{-5}$ and in the vicinity of the Arches and Quintuplet clusters						
240	J174549.35-284919.0	0.4	0.16 ± 0.05	–	–	B
243	J174614.43-284900.0	0.7	0.25 ± 0.08	–	–	S
244	J174616.66-284909.2	0.7	0.26 ± 0.08	–	–	B

NOTE.—The printed version of the table includes only the sources within the *HST* NICMOS fields of the Arches and Quintuplet clusters (Fig. 2s c and d); the full source list is published only electronically. The definition of the bands: 1–2.5 (S1), 2.5–4 (S2), 4–6 (H1), and 6–9 keV (H2). In addition, S=S1+S2, H=H1+H2, and B=S+H. Column (1): Generic source number. (2): *Chandra* X-ray Observatory (registered) source name, following the *Chandra* naming convention and the IAU Recommendation for Nomenclature (e.g., http://cdsweb.u-strasbg.fr/iau-spec.html). (3): Position uncertainty, including an 1σ statistical error calculated from the maximum likelihood centroiding and an approximate off-axis angle (r) dependent systematic error $0\farcs2 + 1\farcs4(r/8')^2$ (an approximation to Fig. 4 of Feigelson et al. (2002)), which are added in quadrature. (4): On-axis source broad-band count rate — the sum of the exposure-corrected count rates in the four bands. (5-6): The hardness ratios defined as HR = (H − S2)/(H + S2), and HR2 = (H2 − H1)/H, listed only for values with uncertainties less than 0.2. (7): The labels "B", "S", and/or "H" mark the bands in which a source is detected; the band which generates the most accurate X-ray centroid position, as adopted in Column (2), is listed first.

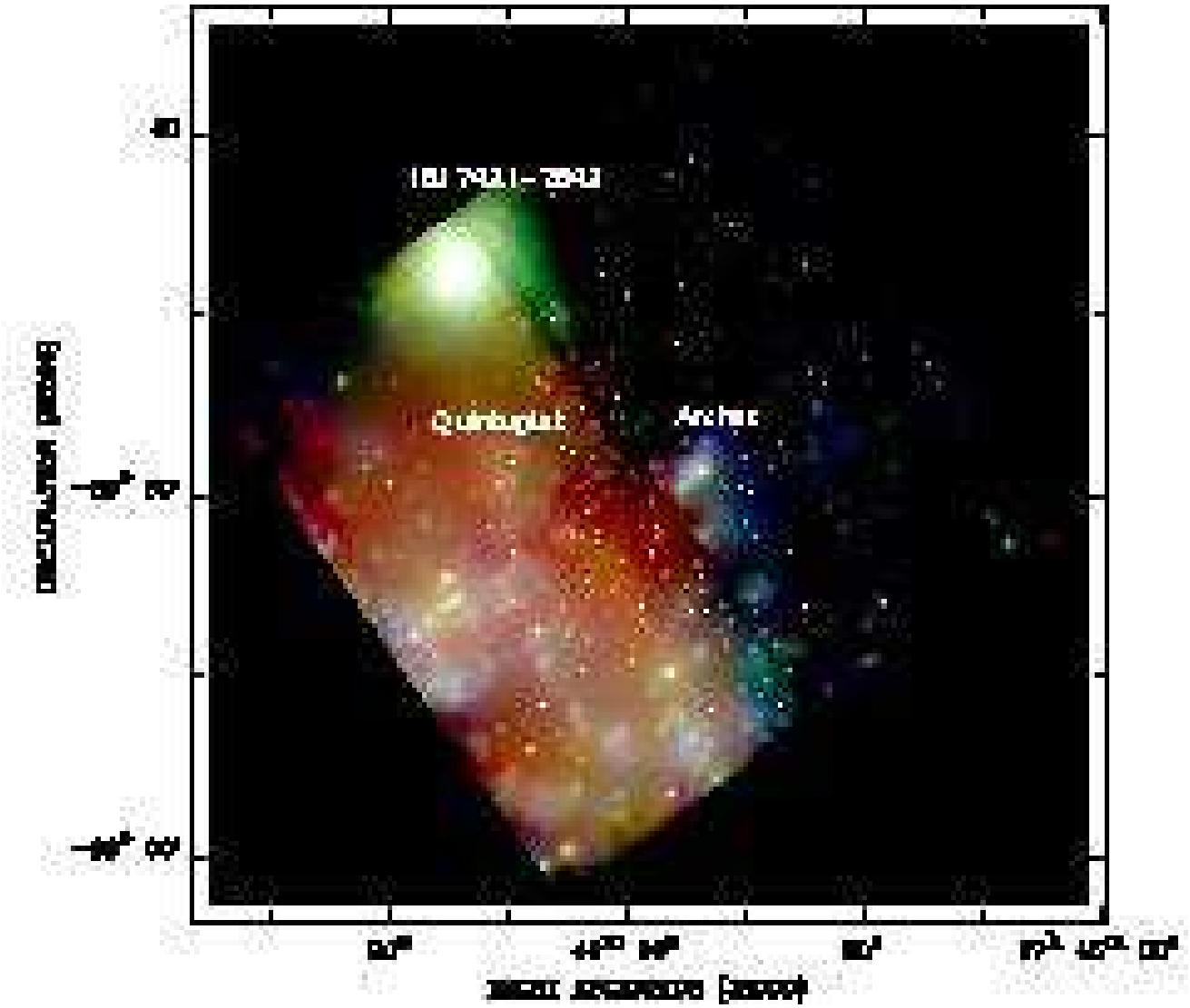

Fig. 1.— Tri-color presentation of the 100 ks *Chandra* ACIS-I observation. Artifacts due to the gaps between the four CCDs and to their outer edge are still visible and are partly caused by sharp changes in the counting statistics.

the ACIS-I field, depending on the local PSF, effective exposure, and background (Wang 2004). Fig. 4 presents the dependence of both the source count rate distribution and the detection completeness on the off-axis distance. The detection limit of the count rate varies from $\sim 1 \times 10^{-4}$ counts s^{-1} near the telescope axis to 10^{-3} counts s^{-1} at the ACIS-I corners. The detection is also subject to the so-called X-ray Eddington bias: more intrinsically faint sources statistically appear to have higher fluxes than the other way around (Wang 2004). We correct for both the incompleteness and bias in our NFR analysis, following the approach detailed in Wang (2004). Briefly, the NFR is analyzed as if it is an X-ray spectrum with the field-integrated incompleteness and flux bias included in the weighted effective area and response matrix.

We first estimate the background AGN contribution in our source detection. We adopt the AGN NFR from the *Chandra* deep surveys in the 2-10 band (Morreti et al. 2003). The energy

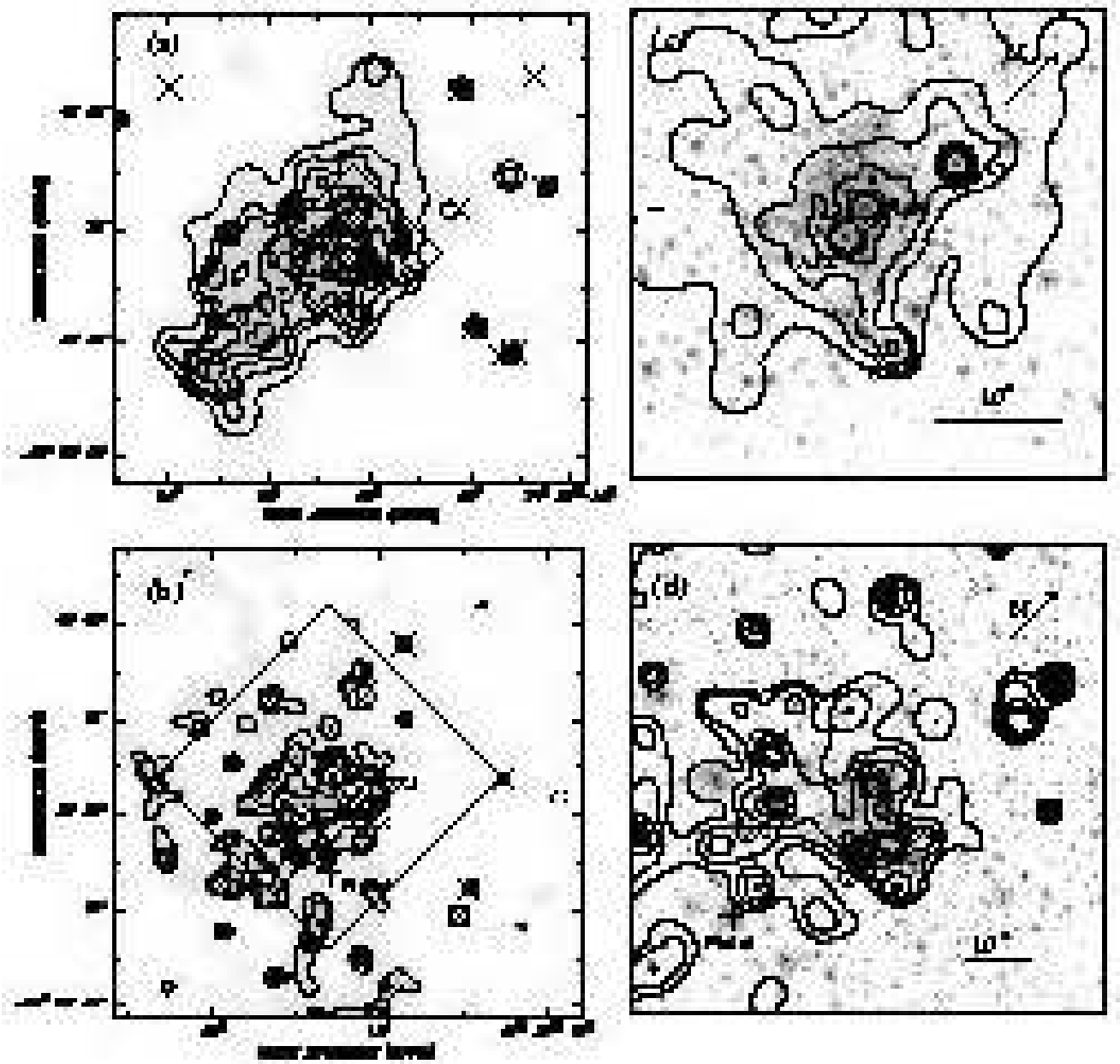

Fig. 2.— ACIS-I 1-9 keV band images of the Arches (a) and Quintuplet (b) clusters. These X-ray images are smoothed with the CIAO routine *csmooth* to achieve a background-subtracted signal-to-noise ratio of ~ 3 (Ebeling et al. 2006). The intensity contour levels are at 20, 23, 27, 33, 43, 57, 80, 180, 482, and 1351 (above a local background of 13.4) for (a), at 17, 29, 33, 42, 54, and 72 (above 17) for (b); all in units of 10^{-3} counts s^{-1} $arcmin^{-2}$. The two large squares in (a) and (b) outline the fields covered by the *HST* NICMOS F205W images of the Arches (c) and Quintuplet (d), respectively (Figer et al. 1999a; Figer et al. 2002). The contours are the same as in (a) and (b), except for excluding the first four levels in (b). The detected sources (Table 1) are marked with *crosses* in (a) and (b). Several bright X-ray sources named previously (Table 2) are labeled.

flux in the NFR is converted into the 1-9 keV band count rate, using the same intrinsic power-

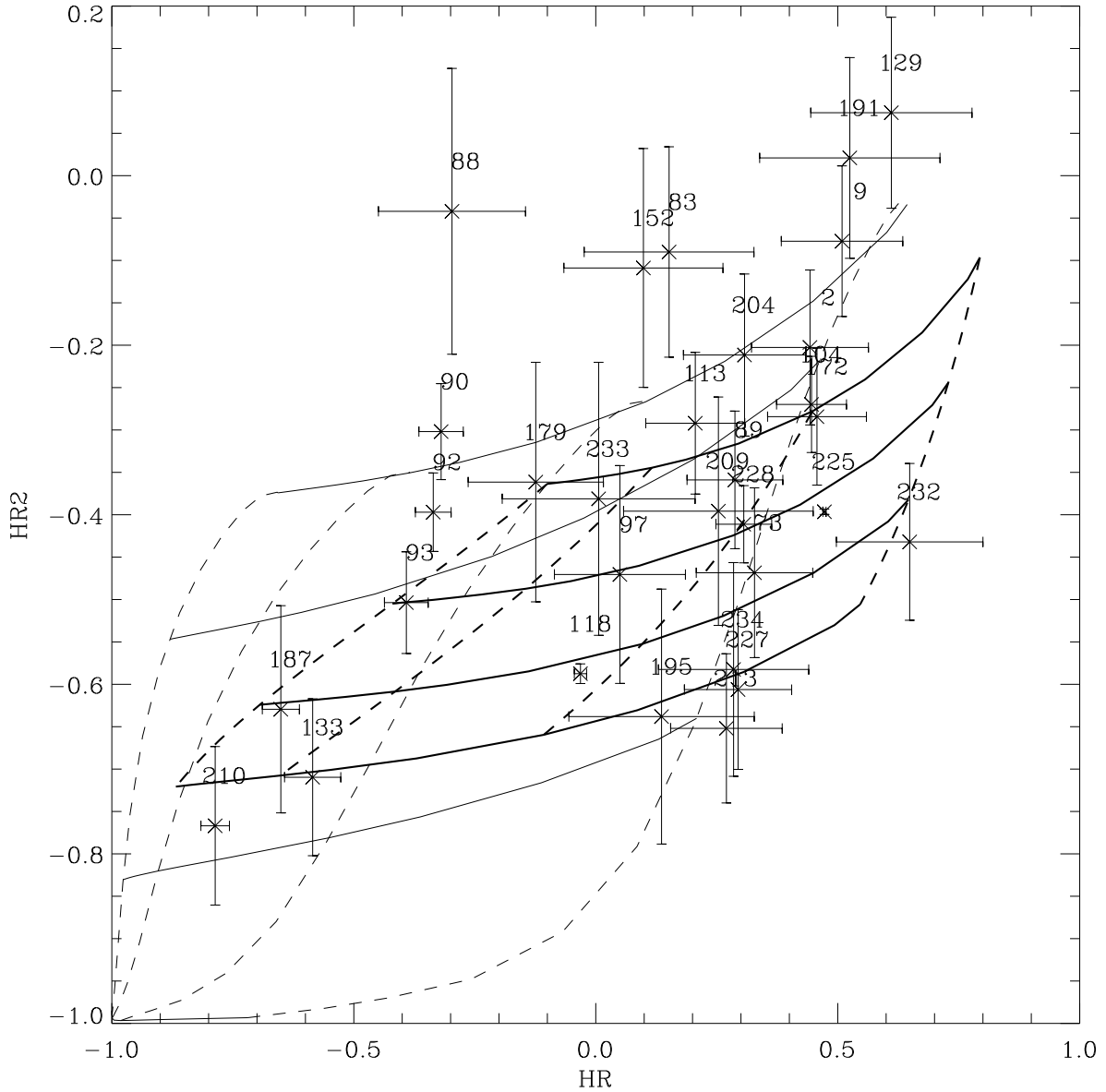

Fig. 3.— Color-color diagrams of X-ray sources with the plotted hardness ratios (HR and HR2) and their 1σ error bars as listed in Table 1. The generic source numbers (Table 1) are marked. Also included in the plot are hardness-ratio models: the solid thick curves are for the power-law model with the photon index equal to 3, 2, 1, and 0, whereas the solid thin curves are for a thermal plasma (XSPEC *MEKAL*; 2×solar metal abundances) with the temperature equal to 0.3, 1, 3, and 6 keV (all from the bottom to the top). The absorbing gas column densities are 1, 3, 10, and 30 $\times 10^{22}$ cm^{-2} for both models (dashed curves from the left to the right).

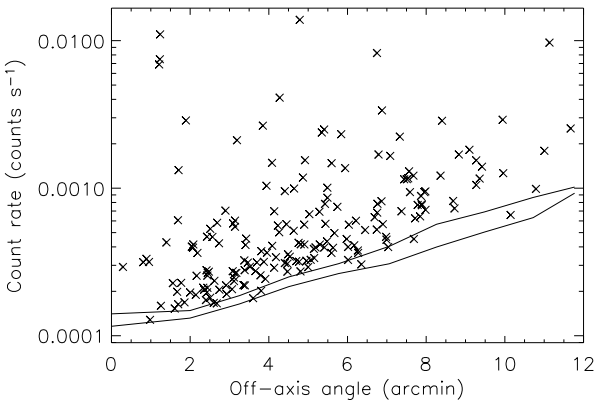

Fig. 4.— Count rates of the sources best-detected in the 1-9 keV band versus their off-axis angles in the 100 ks ACIS-I observation. The curves illustrate the detection thresholds (S_{min}): The upper curve is calculated via an azimuthal average, whereas the lower curve is obtained by choosing the lowest value in each concentric annulus around the aiming point of the observation.

law spectrum with $\Gamma = 1.4$ as assumed in Morreti et al. (2003) and the sight-line absorption $N_H = (1-2)\times10^{23}$ cm^{-2} in our field. Accounting for both the incompleteness and bias, we estimate the corresponding expected number of AGNs in the field to be 18-7, consistent with nine sources preferentially detected in the 4-9 keV band and excluded from our NFR analysis of the sources that are best-detected in the 1-9 keV band.

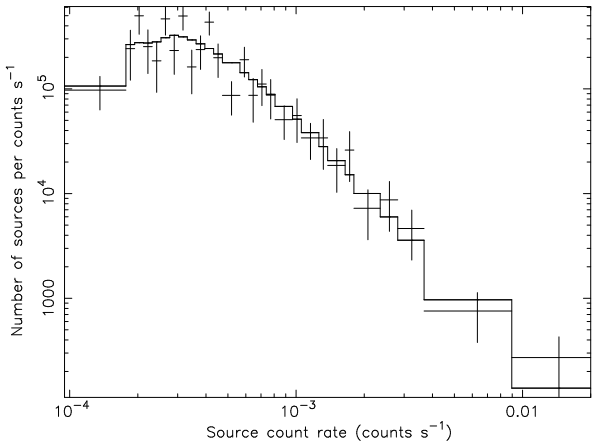

Fig. 5.— Observed differential NFR of the sources best-detected in the 1-9 keV band, compared with the best-fit power-law model. The data are grouped to have a minimum four sources per bin; the fit uses the Cash-statistic and is satisfactory, judged from simulations in XSPEC.

Fig. 5 shows the differential NFR of the all selected sources (as in Fig. 4) and the best-fit power-law

$$\left(\frac{dN}{dS}\right) = AS^{-\alpha-1}, \qquad (1)$$

where S is in units of counts s^{-1}, while $\alpha = 1.28^{+0.14}_{-0.13}$ and $A = 10^{-2.1^{+0.5}_{-0.4}}$ sources per counts s^{-1} (error bars are all at the 90% confidence). To compare with similar results obtained by Muno et al. (2006) for various GC regions, we adopt the same fiducial power law spectrum with $\Gamma = 1.5$ and absorbed by $N_H = 6\times10^{22}$ cm^{-2}. The conversion from the 1-9 keV count rate to the observed 0.5-8 keV photon flux is then 3×10^{-3} (ph cm^{-2} s^{-1})/(counts s^{-1}), while the conversion to the corresponding absorption-corrected flux is 6×10^{-11} (ergs cm^{-2} s^{-1})/(counts s^{-1}). Thus the detection limit of $\sim 1\times10^{-4}$ counts s^{-1} corresponds to a 0.5-8 keV luminosity of 4×10^{31} ergs s^{-1} at the distance of the GC. To get the accumulated NFR, we convert S to the above photon flux, integrate Eq. 1 to infinity, and account for our source detection area of 278 arcmin^2. The resultant accumulated NFR is

$$N(<S) = N_0\left(\frac{S}{S_0}\right)^{-\alpha}, \qquad (2)$$

where the scaling factor $S_0 = 3\times10^{-6}$ ph cm^{-2} s^{-1}, and $N_0 = 0.14$ sources arcmin^{-2}. The above parameter values can be compared to the results based on 28 X-ray sources detected in a 50 ks ACIS-I observation of the radio Arc region (Muno et al. 2006, their Table 2): $N_0 = 0.17$ sources arcmin^{-2} and $\alpha = 1.1\pm0.2$ (1σ error bar), which largely overlaps in field with the present observation. The two analyzes are in good agreement. The slightly low N_0 value in the present analysis is apparently due to our exclusion of both the very soft and hard sources (a factor of 20%). A re-analysis with these sources included confirms this conclusion, but does not change the α value significantly. This insensitivity to the exclusion of the potential foreground and background interlopers indicates that the above estimated NFR is robust.

3.2. Arches Cluster

3.2.1. Discrete X-ray Sources

The X-ray sources, A1N, A1S and A2, stand out in the Arches field (Fig. 6). The reasonably good counting statistics of these sources allow for individual spectral analysis. We extract the on-source spectra from the circle around each source as illustrated in the figure. The spectra of the sources are remarkably similar, in terms of both the overall spectral shape and the presence of the strong 6.7-keV emission line (Fig. 7). A characterization of the spectra with an optically-thin thermal plasma (XSPEC *MEKAL* model) gives statistically consistent temperatures and metal abundances as well as the foreground absorptions (Table 3), although there are significant flux excesses above the model at $\gtrsim 7$ keV, indicating the presence of a harder component (Fig. 7).

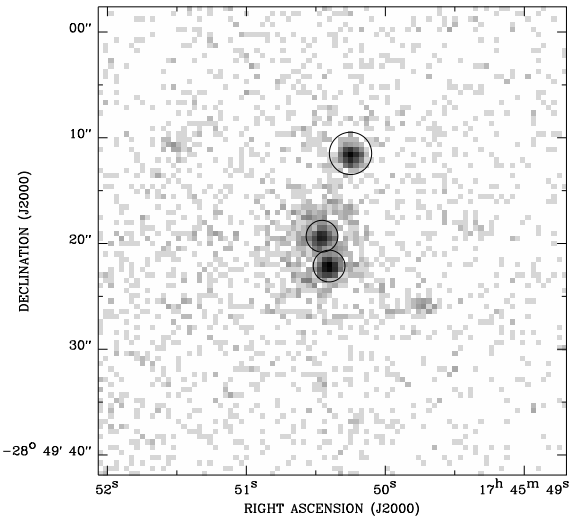

Fig. 6.— ACIS-I close-up of the Arches cluster core. The count image is smoothed with a Gaussian with a FWHM of 0.″3. The circles outlines the regions for the source spectral extractions. Background is extracted within a concentric circle of 50″ radius, excluding the source regions.

To further tighten the constraints on the intrinsic spectral shape, we jointly fit the spectra of the three sources, reasonably assuming that they have the same abundance and absorption, as members of the same stellar cluster. The fit is satisfactory ($\chi^2/d.o.f. = 96/95$; Fig. 7d) and gives the best-fit parameters as N_H=$7.7^{+0.8}_{-0.8} \times 10^{22}$ cm^{-2}, abundance=$1.8^{+0.8}_{-0.2}$ solar, and $kT = 1.8^{+0.2}_{-0.2}$ keV (A1N), $2.2^{+0.4}_{-0.3}$ keV (A1S) and $2.5^{+0.4}_{-0.3}$ keV (A2).

The spectra shown in Fig. 7 represent a substantial improvement in quality than those in Yusef-Zadeh et al. (2002). The on-axis spatial resolution of our new observation allows us not only to separate the spectra of A1N and A1S, but also to minimize the contamination of surrounding diffuse emission (Fig. 6). The calibration of the data has also been improved significantly (e.g., the inclusion of the CTI correction). These improvements probably account for the discrepancies between the present results and those presented in Yusef-Zadeh et al. (2002). Our analysis shows that one-temperature plasma is adequate to fit each of the above spectra and that our inferred total 0.2-10 keV luminosities of the sources are smaller than that of Yusef-Zadeh et al. (2002) by a factor more than 15. These two discrepancies are actually related. The use of the two-temperature plasma model in Yusef-Zadeh et al. (2002) required a very high hydrogen column density ($N_H = 12.4^{+2.9}_{-2.0} \times 10^{22}$ cm^{-2}), which in turn gave a large absorption-corrected luminosities.

3.2.2. Diffuse X-ray Emission

Fig. 2 and 8 show that the enhanced diffuse X-ray emission is distributed over a region greater than the stellar core of the Arches cluster. The diffuse X-ray enhancement is quite isolated within a radius $r \sim 60''$ and is spectrally harder than large-scale diffuse X-ray emission in the region to the southeast (Fig. 1). We extract a spectrum of this enhancement from this radius and a background from a 100″ circle to the west within the same CCD chip. The background-subtracted spectrum of the diffuse emission exhibits significant line emission in the energy range of 6.4 to 6.7 keV. The continuum-subtracted narrow band images of the diffuse emission (§ 2.1) further show that the $\sim$ 6.7-keV line emission arises in a plume from the cluster core (Fig. 10). This plume has a size of $\sim 30''$ at the Arches cluster and elongated toward the northeast. The 6.4-keV line emission is certainly more extended, although its exact extent is difficult to determine; low surface brightness

TABLE 2
IDENTIFICATIONS OF THE X-RAY SOURCES

Source (1)	Source[a] (2)	NIR[b] (3)	Radio[c] (4)
	Arches Cluster		
85	A6	2 (WNL)	AR6+AR10
90	A2	9 (WNL)	–
92	A1S	6 (WNL)	AR1
93	A1N	7 (WNL)	AR4
	Quintuplet Cluster		
214	QX1	242	–
215	QX5	231 (DWCL)	QR7
216	QX2	257 (B0 I)	QR6
217	QX3	211 (DWCL)	–
219	QX4	–	–
244		344 (B1 I-B3 I)	–

[a]Alternative X-ray source names given by Yusef-Zadeh et al. (2002); Law & Yusef-Zadeh (2004).

[b]Near-infrared counterparts: FMS1999 from Figer et al. (1999a) for the Quintuplet and FNG2002 from Figer et al. (2002) for the Arches: WNL - late-type WN stars (WN7-WN9); DWCL - dusty late-type WC stars.

[c]Radio counterparts from Lang et al. (2005).

TABLE 3
SPECTRAL FITS FOR X-RAY SOURCES IN THE ARCHES CLUSTER

Name	$N_H(10^{22}$ cm$^{-2})$	kT (keV)	Abundance	χ^2/d.o.f	L_X[a]	$\log(L_x/L_{bol})$
A1N	$7.3^{+1.5}_{-1.1}$	$1.87^{+0.39}_{-0.32}$	$2.8^{+10.1}_{-1.5}$	16.9/23	7.2	-5.8
A1S	$8.1^{+1.1}_{-1.2}$	$2.1^{+0.58}_{-0.34}$	$1.5^{+1.2}_{-0.6}$	42.2/40	11	-5.7
A2	$6.4^{+2.5}_{-1.6}$	$3.25^{+2.62}_{-1.24}$	$1.6^{+2.1}_{-0.6}$	33.9/28	4.6	-5.9

[a]The luminosity is in units of 10^{33} ergs s^{-1} and in the 0.3-8 keV band.

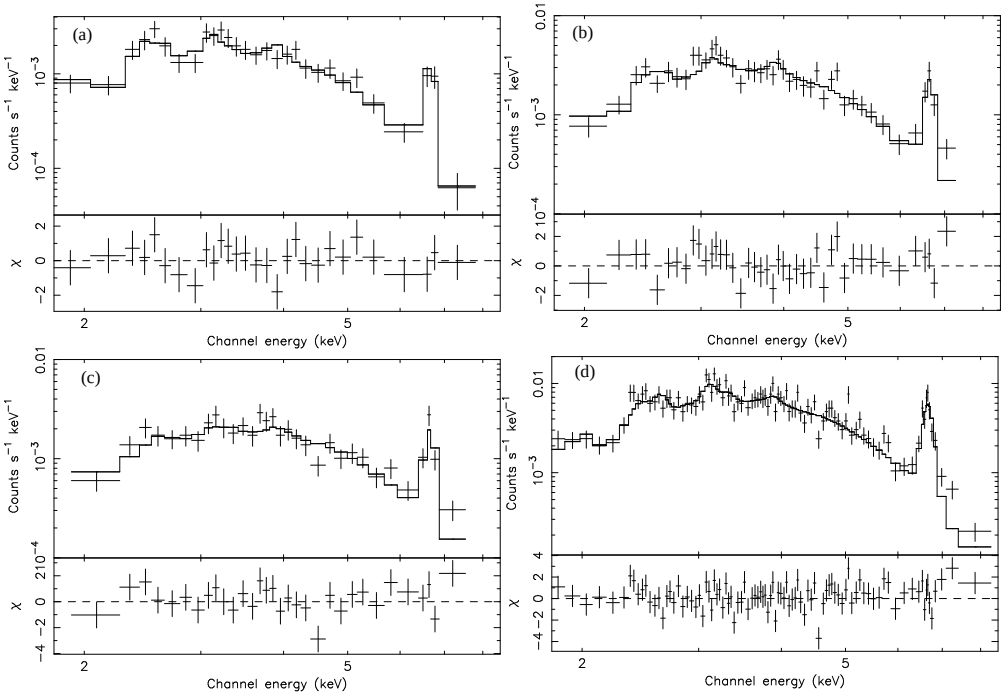

Fig. 7.— ACIS-I spectra of the three brightest X-ray sources in the Arches cluster and the best-fit thermal plasma models: (a) A1N, (b) A1S, (c) A2, and (d) the combination of A1N + A1S + A2. The lower panels show the respective fit residuals relative to the errors of each bin. The spectra are grouped to have at least 20 counts per bin.

6.4-keV line emission of similar EW is ubiquitous in the GC (Wang et al. 2002a). This enhancement of the 6.4-keV line (as well as the continuum emission) around the Arches cluster is particularly strong in an extension from the cluster toward the southeast (SE). The overall morphological appearance of this enhancement is quite irregular (see § 3.4 for a discussion on the possible connection to the adjacent "-30 km s^{-1}" molecular cloud).

We extract two diffuse X-ray spectra: one from the central 6.7-keV line plume, and the other from the SE 6.4-keV line extension from the regions outlined in Fig. 8(a). We fit the spectra with a power law plus a Gaussian line (its width is fixed to zero) to characterize the Fe line centroid and EW, which are $6.60^{+0.10}_{-0.14}$ keV and $1.2^{+1.0}_{-0.9}$ keV for the plume and $6.39^{+0.05}_{-0.05}$ keV and $1.4^{+0.9}_{-0.5}$ keV for the SE extension, respectively. The line and continuum fluxes are 0.25 and 1.3 for the plume, and 0.64 and 2.8 for the SE extension; all in units of 10^{-13} ergs s^{-1} cm^{-2}. The fits are all satisfactory. But the power law component is reasonably constrained only for the SE extension, and the fitted parameters are included in Table 4. The best-fit power law index and line centroid of the SE extension spectrum agree well with the theoretical prediction for the emission from low-energy cosmic-ray electrons interacting with the ambient medium (Valinia et al. 2000; see § 4.4).

While a collisionally ionization equilibrium plasma gives a good fit to the spectrum of the plume (Table 4), the 6.4-keV line in the spectrum of the SE extension may indicate a plasma in a non-equilibrium ionization (NEI) state (see § 4). We thus try a fit of the spectrum with the XSPEC *NEI* model with a metal abundance equal to 2×solar. The fit to the spectrum of the SE extension requires an ionization time scale of $\tau \sim n_e t < 1.1 \times 10^{10}$ cm^{-3} s, too small to be consistent with any dynamic model of the plasma on the observed spatial scale (§ 4).

We further extract a spectrum of the low-surface brightness X-ray emission (LSBXE) from the large circle in Fig. 8a minus the plume and the extension regions. This spectrum (Fig. 9c) also shows both the 6.4-keV line and the He-like S XV

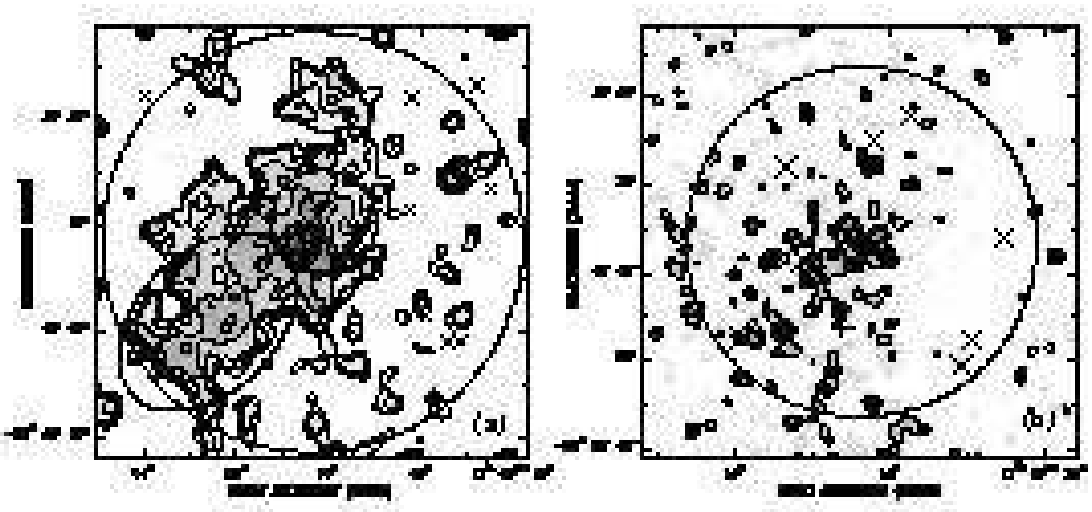

Fig. 8.— Diffuse X-ray emission intensity distributions of the Arches (a) and Quintuplet (b) regions. The excised source positions are marked (see Fig. 2). These X-ray images are adaptively smoothed to achieve a background-subtracted signal-to-noise ratio of ~ 6 to show low-surface brightness emission. The intensity contour levels are at 2.1, 2.3, 2.9, 4.1, 6.4, 11, 21, and 39 (above a local background of 1.8) for (a) and at 3.3, 4.1, and 5.7 (above a local background of ~ 2.5) for (b); all in units of 10^{-3} counts s^{-1} arcmin^{-2}. The large circles in (a) and (b) outline the regions that we use to estimate the total diffuse X-ray emission from the clusters. The two ellipses in (a) outline the regions from which the spectra in Fig. 9 are extracted. The *plus* signs mark the centroid positions of the clusters.

Kα line at ~ 2.5 keV, indicating a mixture of multiple components. Motivated by the above spectral analysis of the plume and the SE extension, we characterize the LSBXE spectrum, using a simple combination of a *MEKAL* plasma, a power law with $\Gamma = 1.3$, and a Gaussian line with its centroid fixed at 6.4 keV. This combination gives a reasonable fit to the spectrum, and the fitted parameters are included in Table 4.

3.3. Quintuplet Cluster

3.3.1. Discrete Sources

Within the field of view of the NICMOS observation (Fig. 2d), we find eight X-ray sources (Table 2). J174614.67-284940.3 is located close to a source candidate first suspected by Law & Yusef-Zadeh (2004) (their QX5 or J174614.7-284947, which should have been named J174614.7-284942). This faint source is now well separated from QX1 and has a near-IR counterpart [FNG2002] 231. Compared to those in the Arches cluster, all of the eight sources are rather faint; in particular, the total number of counts of the four relatively bright sources in the core (QX1-4) is only about 4×10^2. They also show diverse spectral characteristics, as indicated by their significantly different hardness ratios (Table 1). Fig. 11 presents two extreme examples of the source spectra. It is clear that QX1 is very soft, whereas QX4 appears extremely hard. The spectral characteristics of QX2 and QX3 fall between these two extremes. To quantify the diversity, we assume that all these sources have an approximately same intrinsic spectral shape, but have different foreground absorptions. A joint fit of the spectra with a *MEKAL* plasma model (assuming a metal abundance of 2$\times$ solar) gives a characteristic temperature of >8.52 keV and the absorptions along the sight-lines to QX1, QX2, QX3, and QX4 as $N_H(10^{22}\ \mathrm{cm}^{-2}) = 1.3^{+0.5}_{-0.3}$, $4.8^{+2.4}_{-1.3}$, $4.3^{+2.4}_{-1.5}$, and $9.3^{+6.9}_{-3.5}$, respectively. Clearly, the absorption toward QX1 is significantly smaller than toward other sources. Thus QX1 is likely a foreground star. Without a near-IR counterpart, QX4 is likely a background source (e.g., an AGN) or a stellar object that is still deeply em-

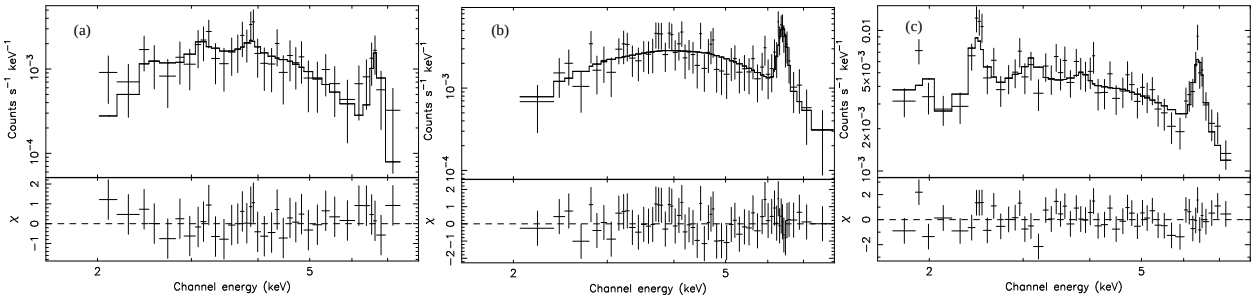

Fig. 9.— ACIS-I diffuse X-ray emission spectra: the 6.7-keV plume (a), the southeast extension (b), and the low-surface brightness outer region (c) of the Arches cluster. The spectra, grouped with a background-subtracted S/N>3, are fitted with the *NEI* for (a), *PL+GAU* for (b) and *MEKAL+PL+GAU* for (c) (Table 4).

TABLE 4
DIFFUSE X-RAY SPECTRAL FITS FOR THE ARCHES CLUSTER

Region	Model	Key Model Parameters	N_H	χ^2/d.o.f	L_X
Central Plume	*NEI*	$kT = 2.56(> 1.18)$, $\tau = 10^{1.1(>0.9)}$	$11.0^{+4.0}_{-2.4}$	12.0/33	3.8
	MEKAL	$kT = 1.88^{+4.19}_{-0.61}$	$10.8^{+5.3}_{-5.6}$	13.3/34	3.2
SE Extension	*PL+GAU*	$\Gamma = 1.3^{+1.4}_{-1.1}$	$6.2^{+2.7}_{-5.6}$	29.2/57	4.1
LSBXE	*MEKAL+POW+GAU*	$kT = 0.45^{+0.25}_{-0.10}$, $\Gamma = 1.3$ (fixed)	$9.2^{+1.8}_{-2.3}$	62.3/52	12

NOTE.—The spectral model names are from XSPEC: *NEI* - non-equilibrium ionization collisional plasma; *MEKAL* - collisional ionization equilibrium plasma; *PL* - power law; and *GAU* - Gaussian line. The metal abundances of plasma is fixed to be 2×solar, as inferred from the point-like source spectra. The plasma temperature (kT), ionization time scale (τ), absorption column density (N_H), and the 2-8 keV luminosity (L_X) are in the units of keV, cm^{-3} s, 10^{22} cm^{-2}, and 10^{33} ergs $^{-1}$, respectively.

bedded in dense gas. QX2 and QX3 do have near-IR counterparts tentatively classified as B0I and dust-enshrouded WCL stars (Table 2). Because of this diversity, we cannot rule out that QX4 is a member of the Quintuplet cluster. We thus fit the combined spectrum of QX2, QX3 and QX4, which have relatively comparable spectral characteristics. The accumulated spectrum shows an emission line at ~ 6.7 keV and can be characterized ($\chi^2/d.o.f. = 34.4/31$) by a *MEKAL* model with $kT = 8.68^{+9.05}_{-3.99}$ keV and a foreground absorption of $N_H = 5.9^{+1.9}_{-1.3}\times10^{22}$ cm^{-2} (Fig. 12), which is consistent with $A_V = 29.0^{+5}_{-5}$ of this cluster (1σ error bar; Figer et al. 1999a), assuming $N_H/E(B-V) \approx 5\times10^{21}$ cm^{-2} mag^{-1} (Bohlin et al. 1978) and $A_V/E(B-V) \approx 2.6-5.5$ (Schlegel et al. 1998). The total absorption-corrected 0.3-8 keV luminosity is 7.6×10^{32} ergs s^{-1}.

3.3.2. Diffuse emission

The extent of the diffuse X-ray enhancement around the Quintuplet cluster is uncertain (Fig. 8). The cluster seems to be embedded in a large-scale diffuse X-ray-emitting region, although the spectrum of the enhancement appears to be slightly harder than that of the surrounding region (Fig. 1). We extract a spectrum of the diffuse emission from a circle of $r = 1'$ radius around the Quintuplet centroid (Fig. 8) and a background spectrum from the field within a concentric annulus of r=1′-2′. The background-subtracted spectrum can be characterized ($\chi^2/d.o.f. = 40.5/34$) by a *MEKAL* plasma model (again assuming a metal abundance of 2×solar) with $kT = 10^{+4.6}_{-2.7}$

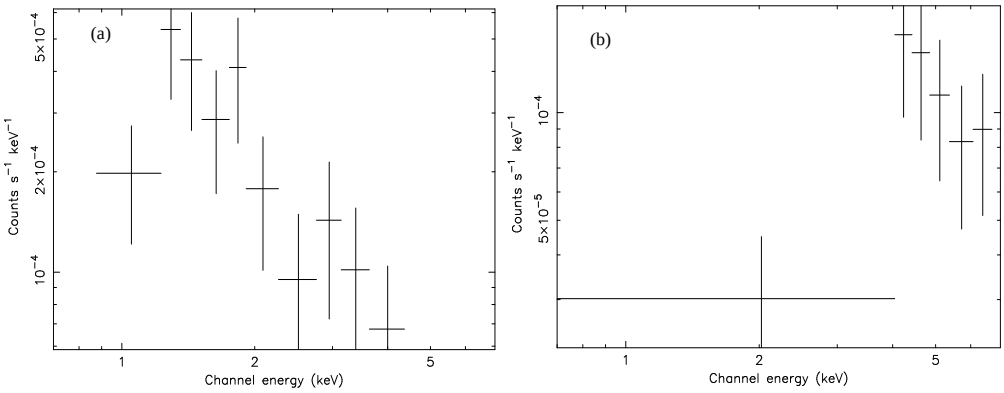

Fig. 11.— Example spectra of X-ray sources in the Quintuplet core: QX1 (a) and QX4 (b).

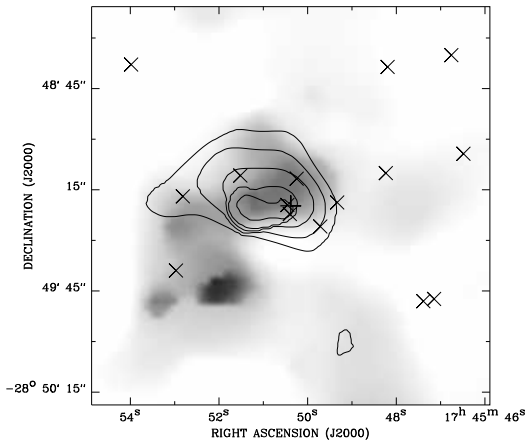

Fig. 10.— ACIS-I 6.4-keV and 6.7-keV line intensity maps of the Arches cluster region. The gray-scale (6.4-keV intensity) is in the range of 0.5 to 4 $\times 10^{-3}$ counts s^{-1} arcmin^{-2} (see also Fig. 14), while the overlaid 6.7-keV line intensity contours are at 0.6, 0.8, 1, 1.2, and 1.6 $\times 10^{-3}$ counts s^{-1} arcmin^{-2}. The *plus* sign marks the centroid position of the cluster.

keV and $N_H = 3.8^{+0.7}_{-0.5} \times 10^{22}$ cm^{-2} (Fig. 13). These parameters are consistent with the values obtained from the fit to the combined spectrum of the discrete sources in the core of the Quintuplet cluster. The absorption-corrected luminosity of the diffuse emission in the 2-8 keV range is 3×10^{33} ergs s^{-1}.

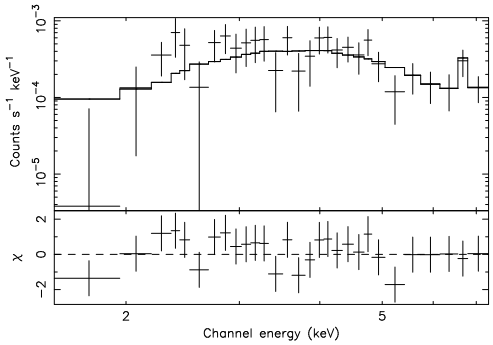

Fig. 12.— Combined ACIS-I spectrum of QX2-4 and the best-fit thermal plasma model.

3.4. Molecular Gas near the Arches Cluster

Fig. 14 presents a comparison of the distribution of the CS (J=2–1) line emission and the 6.4 -keV line emission (Fig. 10). This "clump" of molecular gas represents one of the easternmost parts of the "-30 km s^{-1} cloud" (and corresponds to Peak 2 in the single dish study of this molecular cloud; Serabyn & Gusten 1987). The filamentary molecular cloud has an average velocity of ~ -25 km s^{-1}, although there are large velocity gradients over the cloud and the FWHM of the line is up to ~ 30 km s^{-1}. In contrast, the Arches cluster has an average velocity of $\sim +95$ km s^{-1} (Figer et al. 2002). Therefore, the relative velocity between the cluster and the cloud is at least $v_r \sim 120$ km s^{-1}.

Fig. 14a shows an image of the CS (J=2-1) emission integrated over the central channels,

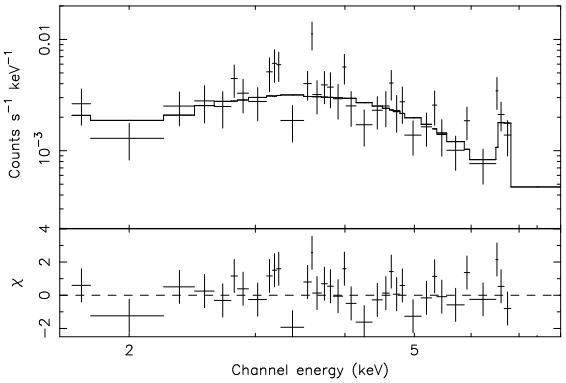

Fig. 13.— ACIS-I spectrum of the diffuse emission in the Quintuplet cluster and the best-fit thermal plasma model.

where the line emission is present (i.e., velocities of -5 to -40 km s^{-1}). Fig. 14b compares this image to the distribution of the diffuse 6.4 keV X-ray emission. There is little morphological similarity between the molecular line emission and the diffuse X-ray emission. The CS intensity is the strongest in the north, where there is little X-ray emission enhancement, either in the broad band or in the Fe Kα lines. Although the 6.4-keV emission appears to coincide spatially with the southern extension of the molecular gas, Fig. 14b shows little peak-to-peak correlation. The individual channel images also reflect this distribution and the lack of detailed physical correlation with the 6.4 keV X-ray emission.

4. Discussion

The above results show distinctly different X-ray properties between the Arches and Quintuplet clusters. The Arches cluster contains three luminous point-like sources, all of which exhibit the strong 6.7-keV emission line, and two apparently diffuse components with either 6.4-keV or 6.7-keV line emission. The 6.4-keV line-emitting enhancement is strongly elongated, morphologically, tracing the east boundary of the CS cloud's southern extension. These characteristics are absent in the Quintuplet cluster, in which we detect only weak X-ray sources, plus a very low surface brightness diffuse emission with a hard spectrum. There is also no evidence for any associated CS cloud. In the following, we discuss origins of these various X-ray components, possible causes of the distinct differences in the X-ray properties between the two clusters, and implications of our results.

4.1. Galactic Center Environment

We attempt to understand the Arches and Quintuplet clusters in the context of the unique GC environment. The generally high gas density and pressure, strong gravitational tidal force, and large random and bulk motion velocities in the GC affect both the formation and evolution of young stellar clusters (Morris 1993). Here we concentrate on the potential interplay between the molecular gas and the Arches cluster.

Is the "-30 km s^{-1} cloud" and the Arches cluster physically associated? On one hand, because of their large velocity separation, the two systems would pass each other in only $\sim 10^4$ yrs if the size of the cloud along the line of sight is comparable to that projected in the sky and at the GC distance. On the other hand, the volume filling factor of dense molecular gas in the region is quite high ($\gtrsim 0.3$; Serabyn & Gusten 1987). In particular, the well-known Arched filaments all have negative velocities similar to that of the molecular gas; the photon-ionization modeling of these filaments suggests that they are physically in the vicinity of the Arches cluster (Lang et al 2001a). Thus the probability for a chance physical contact of a dense cloud with the cluster is not small. An independent argument for the association is an effective extinction deficit of $\delta A_V \approx 10$ over a region of $\sim 15''$ from the cluster core, which can be interpreted as the displacement of the dusty gas by the cluster wind and/or the dust grain destruction by the UV radiation from the cluster (Stolte et al. 2002). The extinction is the largest towards the region just west of the cluster (Stolte et al. 2002; Note that East is to the right in their Figs. 3 and 8). Interestingly, this extinction deficit, corresponding to $\delta N_H \sim 3 \times 10^{22}$ cm^{-2}, provides a natural explanation for the difference between our measured X-ray-absorbing column $N_H \approx 8 \times 10^{22}$ cm^{-2} and the prediction from the total sight-line extinction $A_V = 24$ (Stolte et al. 2002; Bohlin et al. 1978; Schlegel et al. 1998). Furthermore, the interaction of the Arches cluster wind with the cloud may also explain the strong and distinct X-ray emission enhancement around the Arches cluster (§ 4.4). The far-IR spectroscopy further shows the pres-

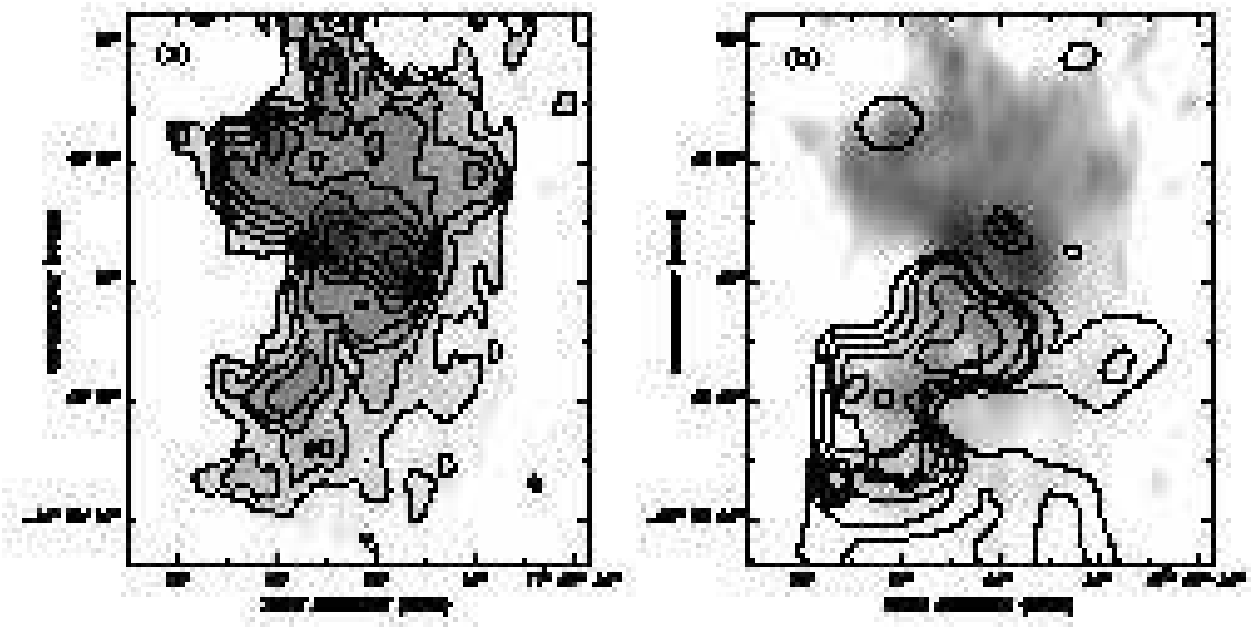

Fig. 14.— (a) Distribution of CS (J=2-1) emission integrated over the central channels, with contour levels representing 9, 12, 15, 18, 21, 24, 27, and 30 Jy beam^{-1} km s^{-1}. (b) The same CS image overlaid with the 6.4-keV line intensity contours at 0.7, 0.9, 1.1, 1.5, 2.1, and 2.9 $\times 10^{-3}$ counts s^{-1} arcmin^{-2}. The *plus* sign marks the centroid position of the Arches cluster.

ence of a component of dusty gas at a velocity of -70 km s^{-1}, unique at the location of the Arches cluster (Cotera et al. 2005). This component may represent shocked cloud gas, deflected toward us (e.g., in the lower left direction of Fig. 16; see § 4.4 for further discussion). Therefore, we tentatively conclude that the "-30 km s^{-1} cloud" and the cluster are undergoing a collision.

The collision of such clouds with the Arches cluster may have strongly affected its evolution. The absence of a natal cloud associated with the cluster at its velocity, for example, may be a consequence of the collision. The removal of this natal cloud from the cluster at an early time could have reduced the probability for low-mass stars to form. The cloud-cloud collision could also be responsible for the formation of the Arches cluster itself. The exceptionally high gas temperature and velocity dispersion in such a formation formation process could also result in a top-heavy initial mass function (IMF; see § 4.5 for further discussion).

Our X-ray study further provides useful measurements about the GC environment. In addition to the N_H measurement, we have also directly estimated the metal abundance (mainly iron) in the GC. Recent estimates based on near-IR spectroscopy of young and intermediate-age supergiants in GC (e.g., Ramírez et al. 2000) suggest an iron abundance that is consistent with being solar, i.e., similar to the abundance observed in the solar neighborhood. This result is *against* the general trend of an increasing metallicity with decreasing galacto-centric radius as observed in the disks of the Milky Way and nearby galaxies. Our X-ray measured iron abundance of $\sim 1.8^{+0.8}_{-0.2}$ solar, based on the spectral analysis of the luminous colliding wind candidates in the Arches cluster, agrees with the trend. The thermal process involved in the X-ray emission is quite simple, and the ion fraction of the He-like Fe Kα emission is insensitive to the exact plasma temperature fitted. Furthermore, the iron abundance in the winds of the massive stars is not expected to be contaminated by their own nuclear synthesis in the deep cores of the stars. Therefore, we conclude that the iron abundance in the ISM of the GC is super-solar.

4.2. Nature of Discrete X-ray Sources

As shown in § 3.1, our analysis confirms a relatively flat source NFR in the region of the Arches and Quintuplet clusters, as indicated first in Muno et al. (2006). Our obtained power law slope ($\alpha = 1.26^{+0.14}_{-0.13}$; 90% confidence) is flatter than those in the deep observations of Sgr B2 (1.7 ± 0.2) and Sgr A* (1.4 ± 0.1) as well as the $2^\circ\times0.^\circ8$ shallow survey (1.5 ± 0.1). The implied over-population of relatively bright X-ray sources is clearly related to the presence of the two clusters.

The discrete X-ray sources in the core of the clusters are unlikely due to emission from individual normal massive stars or even binaries. The X-ray emission from such a star/binary can be characterized typically by an optically-thin thermal plasma with a temperature of $\sim$ 0.6 keV and a luminosity following the empirical relation $\frac{L_X}{L_{bol}} \sim 10^{-7}$, where L_{bol} is the bolometric luminosity. Thus the emission is too soft and faint to be observed from the GC. Even the Pistol star near the core of the Quintuplet cluser (Fig. 2d) is not detected as an X-ray source. The star is a luminous blue variable with $L_{bol} \gtrsim 10^{6.6} L_\odot$ and has an extinction of $A_K \approx 3.2$, corresponding to $N_H \approx 5.1 \times 10^{22}$ cm^{-2}. Assuming the *MEKAL* thermal plasma with a temperature of 0.6 keV, we estimate that the 3σ upper limit to the 0.3-8 keV luminosity is 3×10^{33} ergs s^{-1}, consistent with $L_x/L_{bol} \sim 10^{-7}$.

Most likely, the luminous X-ray sources associated with the Arches cluster represent colliding stellar winds in massive star close binaries. The characteristic shock temperature of a colliding wind is

$$T \simeq (3 \times 10^7 \text{ K}) v_{w,3}^2, \quad (3)$$

where $v_{w,3}$ is the relative colliding wind velocity in units of 10^3 km s^{-1}. Well-known examples of such systems are WR11 (kT$\approx$ 4.3 keV, $L_X \sim 8 \times 10^{33}$ ergs s^{-1}; Schild et al. 2004) and WR140 (kT$\approx$ 3 keV, $L_X \sim 2 \times 10^{33}$ ergs s^{-1}; Zhekov et al. 2000). Clearly, the expected temperatures are similar to the measured values for the sources in the Arches cluster, although their luminosities seem to be substantially higher than those confirmed colliding wind systems, which all have $L_X < 1\times10^{34}$ ergs s^{-1} (e.g., Oskinova 2005). The unusually high X-ray luminosities of the colliding wind systems may be related to the compactness of the Arches cluster, in which very close binaries may form dynamically.

In contrast, the X-ray sources in the Quintuplet cluster are probably typical colliding wind systems. They all have individual L_X in the range of $(0.2 - 3) \times 10^{33}$ ergs s^{-1} as well as the hard X-ray spectra with the 6.7-keV emission line, as expected.

While only relatively luminous X-ray sources are detected individually, sources below our detection limit are hidden in the "diffuse" emission. Indeed, the diffuse emission in the cores of the Arches and Quintuplet clusters shows a general correlation with their stellar distributions (Fig. 15). Thus, relatively faint colliding wind binaries could significantly contribute to the emission. But the bulk of the diffuse X-ray emission in outer regions of the clusters may have different origins for several reasons. First, the emission extends much further away from the cluster cores than the stellar light distributions (Fig. 15). Second, the spectrum of the diffuse emission is harder than that of the discrete sources. Third, the emission in the outer region of the Arches cluster mainly exhibits the 6.4-keV line, inconsistent with the the colliding wind interpretation.

4.3. Cluster Winds

In addition to colliding winds in individual massive star binaries, the collision among stellar winds collectively becomes important in a compact cluster such as the Arches. The collision results in the thermalization of the stellar winds and their subsequent merging into a so-called cluster wind. Various 1-D models and 3-D hydrodynamic simulations have been carried out on cluster winds (Raga et al. 2001; Stevens & Hartwell 2003; Rockefeller et al. 2005). Within the uncertainties of such model parameters as overall stellar wind velocities and mass loss rates, simulated cluster winds are shown to explain the luminosities of diffuse X-ray emission from several star clusters (e.g., Stevens & Hartwell 2003; Rockefeller et al. 2005); but little detailed comparison has yet been performed.

Fig. 15 compares the radial diffuse X-ray intensity profiles from the 3-D hydro-dynamical simulations, carried out specifically for the Arches and Quintuplet clusters, approximately accounting for

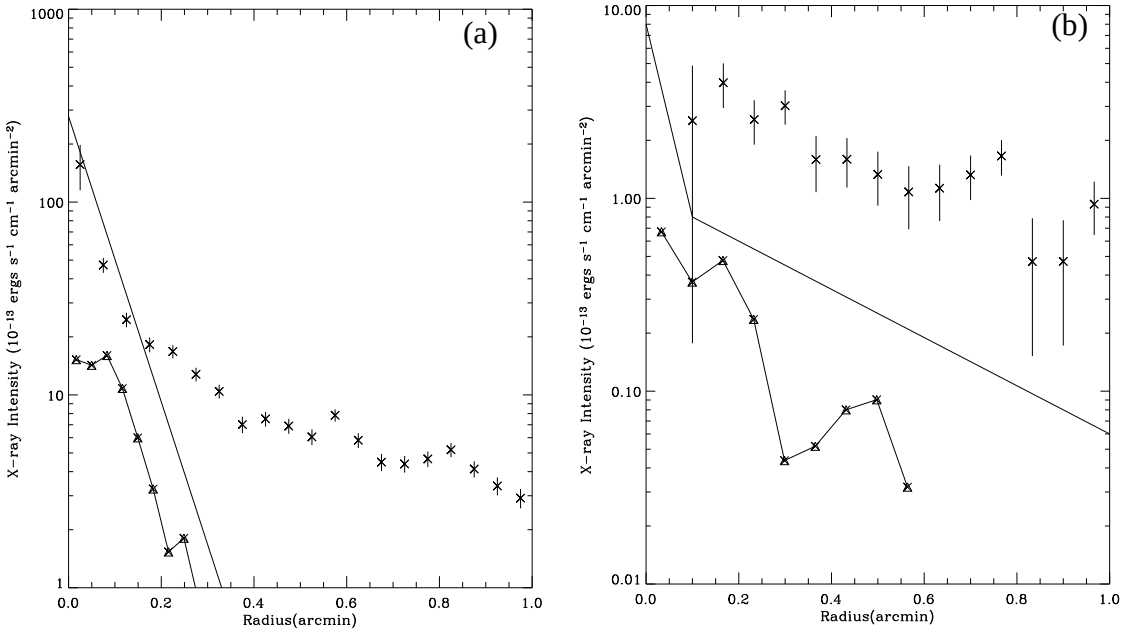

Fig. 15.— Radial ACIS-I 1-9 keV intensity profiles (*crosses* with 1σ error bars) around the Arches (a) and Quintuplet (b) clusters, compared with the respective NICMOS F205W stellar light distributions (connected *triangles*). The cluster wind predictions are shown approximately as the solid line from 3-D simulations for the "standard" stellar wind mass-loss rates of the two clusters (Rockefeller et al. 2005).

the discrete positions of massive stars and their individual stellar wind properties (Rockefeller et al. 2005). For the Quintuplet, the cluster wind could account for $\sim 1/4 - 1/3$ of the observed diffuse X-ray emission. For the Arches, which is much more compact, the simulated profile gives a reasonably good match to our measured distribution of the diffuse X-ray intensity within $\sim 10''$, but is too steep to explain the emission at larger radii. The flattening of the observed intensity distribution in the radius range of $\sim 10''$ to $\lesssim 15''$) may arise from the reverse shock heating and confinement of the wind. At larger radii, the overall diffuse X-ray enhancement demonstrates a bow shock morphology and is prominent in the Fe Kα 6.4-keV line emission (§ 3.2.2), inconsistent with the expectation for the cluster wind interpretation (see below). Therefore, the cluster wind may be important in the core, but not in the outer region of the Arches cluster.

The complexity of the diffuse X-ray emission from the Arches cluster probably reflects its interaction with the CS cloud. Both the morphology of the diffuse X-ray emission, particularly the elongation of the 6.7-keV line emission, and the extinction deficit distribution indicate that the motion of the cluster relative to the cloud is from East to West in the sky. Because of their supersonic relative motion, a bow-shock is expected to form around the cluster. Fig. 16 illustrates this simple-minded scenario for the interaction, although the true situation is certainly more complicated.

Following van Buren & McCray (1988), we can estimate from the ram-pressure balance the characteristic radius of the reverse shock in the cluster wind as

$$r_s = (0.7 \text{ pc}) \dot{M}_{w,-4}^{1/2} v_{w,3}^{1/2} v_{r,2}^{-1} n_{a,2}^{-1/2}, \qquad (4)$$

where $\dot{M}_{w,-4}$ is the mass-loss rate of the cluster wind (in units of $10^{-4} M_\odot$), $v_{r,2}$ is the relative velocity between the cluster and the cloud (10^2 km s^{-1}), and $n_{a,2}$ is the gas density in the colliding cloud (10^2 cm^{-3}). Because the contact discontinuity has a scale $l_c \sim 1.5 r_s$, we can estimate the volume of shocked wind materials as $V \sim \frac{4\pi}{3}(1 - 1/1.5^3) l_c^3$. Assuming that this volume

corresponds to the 6.7-keV line plume, which has a radius $l_c \sim 0.6$ pc ($15''$) and we can infer $n_e \sim 5$ cm^{-3} from the integrated emission measure of the central plume, $IEM \sim 16$ cm^{-6} pc^3 (the *MEKAL* fit in Table 4). The ram-pressure balance also gives the density of the shocked ambient gas $n_a \sim \frac{n_e}{4}(\frac{v_w}{v_r})^2 \sim (1.3 \times 10^2 \text{ cm}^{-3}) v_{w,3}^2 v_{r,2}^{-2}$. This, together with Eq. 4, gives $\dot{M} \sim (1 \times 10^{-4} M_\odot) v_{w,3}$.

The above inferred n_a and $\dot{M}$ values depend on v_w, which may be quite uncertain. In particular, the near-IR spectroscopic estimate of stellar winds may have significantly underestimated v_w as possible low-emissivity winds in the line profiles were not taken into account (Cotera et al. 1996), i.e., the wind terminal velocity could be considerably higher than 1×10^3 km s^{-1}. Nevertheless, the above inferred mass-loss rate still appears substantially smaller (by a factor of up to ~ 10) than the current estimates based on radio continuum estimates (e.g., Lang et al. 2005). Such estimates may be very uncertain (e.g., Rockefeller et al. 2005), particularly for binaries with strong wind-wind interaction. The relatively small n_a value is consistent with the weak CS emission from the ambient gas, probably representing the inter-clump medium of the colliding cloud.

While the shocked cluster wind should be constantly flowing out from the bow shock at a velocity comparable to the sound velocity $c_s \sim (8 \times 10^2 \text{ km s}^{-1}) v_{w,3}$, we can also estimate the ionization time scale as $\tau \sim n_e l_c / c_s \sim (1 \times 10^{11} \text{ cm}^{-3} \text{ s}) v_{w,3}^{-1}$, which is much too large to explain the 6.4-keV line emission with an *NEI* plasma, but is consistent with that inferred from the spectrum of the central plume (§ 3.2.2). Therefore, the observed size and shape of the 6.7-keV line plume (Fig. 10), at least qualitatively, match the predictions of this simple bow shock interpretation, within the uncertainties of the relevant parameters.

4.4. Origin of the 6.4-keV line emission

The above discussion indicates that the 6.4-keV line emission associated with the Arches cluster is unlikely due to an *NEI* process. We thus consider the possible origin of the line emission as the filling of iron K-shell vacancies produced by either ionizing radiation with photon energies > 7.1 keV or collision with low-energy cosmic-ray electrons (LECRe; Valinia et al. 2000). The fluorescent line emission and Thompson continuum scattering seem to give a reasonable good explanation for those most prominent 6.4-keV enhancements associated with well-known giant molecular clouds such as Sgr B2 and Sgr C in the GC (Koyama et al. 1996; Cramphorn et al. 2002; Revnivtsev et al. 2004). This explanation requires the presence of a luminous X-ray source with a spectrum consistent with the observed power law continuum with a photon index of $\Gamma \approx 1.8$. Because such a source is currently not present in the GC, the observed emission is proposed to be the reflection of past Sgr A*, with an X-ray luminosity of $\gtrsim 10^{39}$ ergs s^{-1}, about a few hundreds years ago.

However, the fluorescence interpretation has difficulties in accounting for the 6.4-keV line emission regions closer to Sgr A*. A comparison of the CS emission and the diffuse 6.4-keV line intensity does not show a peak-to-peak correlation, which should be expected because the gas traced by the CS emission is expected to be optically thin to the iron ionizing radiation (Wang 2003). As shown in § 3.4, the detailed correlation is also absent in the Arches CS cloud. This difficulty may be avoided, if the CS emission does not trace well the actual gas distribution (e.g., due to the destruction of the molecule by the strong UV radiation from the Arches cluster). Even in this case, however, the gas column density of the cloud cannot be much greater than $\delta N_H \sim 10^{22}$ cm^{-2}, constrained by both the X-ray absorption and the near-IR extinction distribution (§ 4.1). Following Sunyaev et al. (1998), we estimate the required X-ray luminosity of Sgr A* to produce the detected 6.4-keV line intensity of the Arches (Fig. 14) as

$$L_X = (4 \times 10^{39} \text{ ergs s}^{-1})(d/27 \text{ pc})^2 (\delta N_H / 10^{22} \text{ cm}^{-2})^{-1}, \quad (5)$$

where we have assumed the iron abundance to be $2 \times$ solar and have scaled the distance (d) between the cloud and Sgr A* to be their projected separation in the sky, corresponding a light travel time of only about 90 years. Of course, the actual distance is likely to be greater, and the required L_X should then be higher. This common interpretation of the 6.4-keV line enhancement and those associated with Sgr B2 and Sgr C, though difficult to rule out completely, would not explain the apparent position coincidence between the cloud and the cluster.

Alternatively, one may consider the Arches cluster as the origin of the hard X-rays. But this possibility can be easily dismissed because of the absence of the 6.7-keV line (which is strong in both the point-like sources and in the cluster core) in the 6.4-keV line enhancement. Furthermore, the observed X-ray luminosity of the cluster is more than a factor of 10^2 short of what is required for the fluorescence interpretation.

A more plausible scenario for the Arches 6.4-keV line enhancement is the LECRe-induced Fe K-shell vacancy filling (Valinia et al. 2000). In this scenario, the continuum is due to the bremsstrahlung radiation of the LECRe. The expected power-law photon index of the continuum is 1.3-1.4 over the range of 1-10 keV, consistent with our measured value of the SE extension (Table 4). The LECRe may be produced in strong shocks that are present within the Arches cluster and in both the forward bow shock and the reverse-shock in the cluster wind (see the discussion above). For example, Bykov et al. (2000) have shown that a shock of velocity $\gtrsim 10^2$ km s^{-1} into a molecular cloud, accompanied by magneto-hydrodynamic turbulence, can provide a spatially inhomogeneous distribution of nonthermal LECRe. Yusef-Zadeh et al. (2003) have further presented observational evidence for nonthermal diffuse radio emission from the Arches cluster and have suggested that colliding wind shocks may generate the responsible relativistic particles. The diffuse X-ray enhancement has a bow-shock morphology and is presumably linked to the site of particle acceleration. But, because of particle diffusion and gas flow, one does not expect a peak-to-peak correlation of the X-ray emission with the CS emission from the colliding cloud. Following Yusef-Zadeh et al. (2002a), we estimate the LECRe energy density required to produce the observed 6.4-keV line intensity. If the *shocked* gas density is $\sim 10^3$ cm^{-3}, the required energy density is then $\sim 6 \times 10^3$ eV cm^{-3}, substantially greater than the value 0.2 eV cm^{-3} from averaging over the Galactic ridge (Valinia et al. 2000). But the implied pressure inside the bow shock can still be balanced by the high ram-pressure ($\sim 2 \times 10^{-8} v_{r,2}^2 n_{a,2}$ dyn cm^{-2}) of the collision between the cluster wind and the CS cloud. In short, the bow shock provides a plausible interpretation of the distinct spatial and spectral properties of the diffuse X-ray emission around the cluster and its physical relationship to the CS cloud.

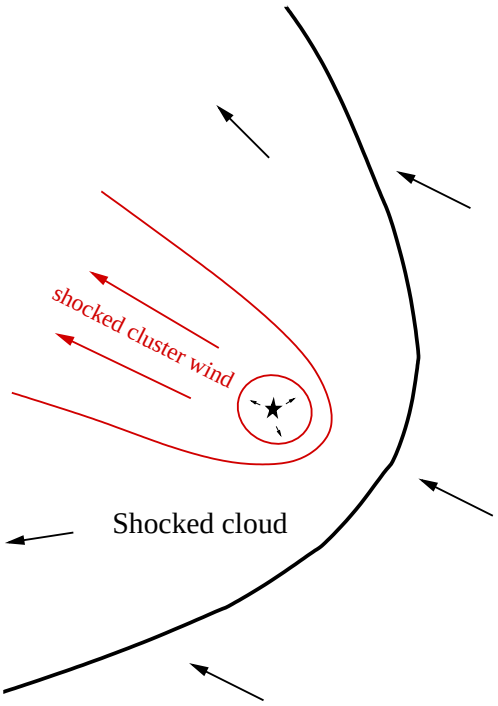

Fig. 16.— An illustration of the proposed cluster-cloud collision scenario for the Arches. The shocked cloud gas is partly traced by the CS and 6.4-keV lines (Fig. 14), whereas the shocked cluster wind plasma near the cluster is by the 6.7-keV line (Fig. 10).

Finally, we consider the possibility that the 6.4-keV line enhancement represents the reprocessed X-rays from numerous discrete and faint sources embedded around the Arches cluster. A natural candidate for such sources might be low-mass pre-main sequence young stellar objects (YSOs). But they are in general not known to emit strong 6.4-keV line emission. In the Orion nebula, for example, the line emission is detected from only a few YSOs and with EWs less than 300 keV. Therefore, YSOs are probably not a significant contributor to the 6.4-keV line enhancement.

4.5. YSO population and stellar IMF

The overall luminosity of the diffuse X-ray emission provides a fundamental limit to the population of YSOs and hence the IMF of the Arches and Quintuplet clusters. YSOs in the mass range

of $(0.3-3)M_{\odot}$ typically have large L_X/L_{bol} ratios and hard X-ray spectra. Most importantly, they can be numerous, as shown in the *Chandra* Orion Ultra-deep Project (Feigelson et al. 2005). Though with a *mean* 2-8 keV luminosity of only $\sim 1.2\times10^{30}$ ergs s^{-1} per star, YSOs collectively account for about 75% of the luminosity of the Orion nebula, the IMF of which is consistent with the standard Miller & Scalo (1979; MS hereafter), based on the work by Hillenbrand (1997). If the clusters in the GC have a similar IMF, YSOs should then be equally important.

At the GC, typical YSOs cannot be detected individually, but can be constrained collectively in *Chandra* observations. Based on the diffuse X-ray intensity observed around Sgr A*, Nayakshin et al. (2005) find that the population of YSOs in the GC cluster is extremely small. They conclude that it cannot be a remnant of a massive star cluster, originated at several tens of parsecs away from Sgr A* and then dynamically spiralled in, and is thus most likely formed *in situ* in a self-gravitating circum-nuclear disk and with a top heavy IMF. While star formation around a super-massive black hole represents an extreme, it is clearly important to examine the IMF of the Arches and Quintuplet clusters in the general environment of the GC.

We find a similar deficiency of YSOs in Arches and Quintuplet clusters, which places important constraints on their IMF. Existing near-IR studies have provided estimates on the present-day MF of stars with masses greater than a few solar masses in the core of the Arches cluster; MF measurements in outer regions are difficult because of severe confusion with field stars. Fig. 17 shows the MF within $r < 0.4$ pc of the Arches cluster (Stolte et al. 2005), compared with various predictions of YSOs. The standard MS IMF, normalized with the number of stars in the mass range of $M > 60$ M$_{\odot}$, predicts at least 2×10^5 YSOs. Using our measurements of the diffuse X-ray emission, we can directly get an upper limit to the population of YSOs over the entire cluster ($r < 2.5$ pc). We assume that the mean X-ray luminosity of the YSOs in the Arches cluster to be the same as that in the Orion nebula, because of their similar ages. As is shown above, much of the diffuse X-ray emission, though difficult to quantify, likely has other origins (e.g., cluster winds) to account for the prominent iron Kα lines. Therefore, the use of the total 2-8 keV diffuse X-ray luminosity of 2×10^{34} ergs s^{-1} (Table 4) gives the upper limit as 2×10^4 YSOs, which is a factor of 10 smaller than the above prediction from the MS IMF. The actual discrepancy should be substantially larger. We have neglected the mass loss in the stellar evolution, which is important for the massive stars. Considering the mass loss, the number of stars in the above initial mass range, hence the normalization of the IMF, would be greater. The number of cluster stars in the region of $r = 0.4-2.5$ pc is also not included, though difficult to fully quantify; for example, there are 77 stars with $M > 40M_{\odot}$ in the radius $r < 0.6$ pc (Figer et al. 1999b), compared to about 48 in the same mass range of the MF obtained by Stolte et al. (2005) for $r < 0.4$ pc.

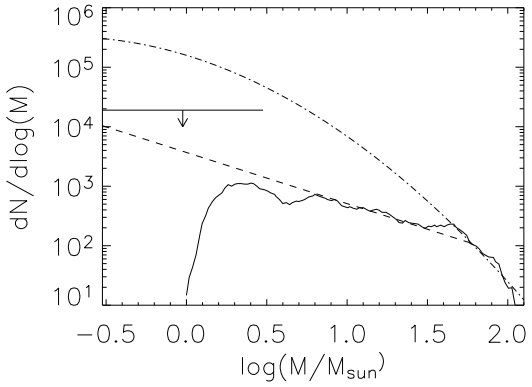

Fig. 17.— Present-day MF as obtained by Stolte et al. (2005) in the $r < 0.4$ pc core of the Arches cluster, compared with the power law ($\propto M^{\Gamma}$, where $\Gamma = -0.86$; dashed curve) fitted in the 6-60 M$_{\odot}$ range (Stolte et al. 2005)) and the MS half-Gaussian (dot-dashed line), normalized to the number of stars in the mass range of > 60 M$_{\odot}$. The X-ray-inferred upper limit to the number of YSOs (0.3-3 M$_{\odot}$) in the entire cluster is marked as the bar with the arrow. The MF at M $\lesssim 6$ M$_{\odot}$ may be significantly contaminated by field stars (Stolte et al. 2005).

An extrapolation of a power law fit in the mass range of 6-60 M$_{\odot}$, as obtained by Stolte et al. (2005), is consistent with the X-ray-inferred number of YSOs (Fig. 17). But, Stolte et al. (2005) shows that the MF steepens with radius. This steepening is expected as a result of the dynamic

mass segregation of stars in the cluster core (Kim et al. 2002; Portegies Zwart et al. 2002). Furthermore, mergers among stars may also be important in flattening the MF toward the cluster core. Therefore, the MF of the entire cluster, including the region in $r = 0.4 - 2.5$ pc, is likely to be steeper. If this is the case, a turnover in the MF (e.g., at ~ 6 $M_\odot$, as indicated in the study of Stolte et al. (2005), may indeed be required to explain the X-ray-inferred upper limit on the overall YSO population in the Arches cluster.

Similarly, we can constrain the YSO population in the Quintuplet cluster. There are 30 stars with masses larger than 20 $M_\odot$ within $r = 25''$ (1 pc) of the Quintuplet cluster (Figer et al. 1999a). Assuming the MS IMF would predict a total number of YSOs to be at least 2×10^4. These YSOs would have a 2-8 keV luminosity of $\sim 1 \times 10^{34}$ ergs s^{-1}, accounting for the weak dependence of the mean X-ray luminosity on the cluster age (a factor of 1.6; Preibisch et al. 2005). This predicted value is a factor of 5 greater than our measured total diffuse X-ray luminosity of 2×10^{33} ergs s^{-1} within $\sim 1'$ of the Arches2 cluster (§ 3.2.2).

5. Summary

We have presented a deep *Chandra* ACIS-I observation of the Arches and Quintuplet clusters. This observation, complemented by a high-resolution OVRO mapping of a CS cloud accompanied with the Arches cluster, allows for an in-depth study of the high-energy phenomena and processes in these two clusters and their interplay with the GC environment. The main results of our study are as follows:

- Point-like X-ray sources in the *Chandra* observation are detected down to a detection limit of $\sim 5 \times 10^{31}$ ergs s^{-1} in the 1-9 keV band. This list should contain all significant massive colliding wind binaries in the ACIS-I field. The superb *Chandra* positioning of these sources allow for identifications of multi-wavelength counterparts. We consider those sources best-detected in the 1-9 keV band to be likely located in the GC, whereas those sources preferentially detected in the 1-4 keV or 4-9 keV band are good candidates for foreground stars or extragalactic AGNs. In particular, we estimate that the AGN contribution is on the order of only a few % of all our detected X-ray sources.

- The X-ray source number-flux relation of the Arches and Quintuplet cluster region can be characterized by a power law $N(< S) = N_0(S/S_0)^{-\alpha}$, where $N_0 = 0.14$ sources arcmin^{-2}, $\alpha = 1.26^{+0.14}_{-0.13}$, and $S_0 = 3{\times}10^{-6}$ ph cm^{-2} s^{-1}, equivalent to 6×10^{-14} ergs cm^{-2} s^{-1}, in the 0.5-8 keV band. This relation is significantly flatter than those determined in other regions of the GC (Muno et al. 2006), apparently due to the presence of a massive star-related population of relatively bright X-ray sources.

- The three bright point-like X-ray sources in the core of the Arches cluster show remarkably similar spectra, which can all be characterized by an optically-thin thermal plasma with a temperature of $\sim 1.8 - 2.5$ keV, a metal abundance of $\sim 1.8^{+0.8}_{-0.2}$ solar, and a foreground absorption of $7.7^{+0.8}_{-0.8}{\times}10^{22}$ cm^{-2}. The 0.3-8 keV luminosities of the sources are in the range of $(5 - 11) \times 10^{33}$ ergs s^{-1}. The sources have near-IR counterparts as late-type WN stars, which tend to have massive and fast stellar winds. Therefore, the sources likely represent the extreme examples of colliding stellar wind binaries. The measured super-solar metal (iron) abundance is consistent with other X-ray measurements of thermal hot plasma in the GC environment.

- The X-ray sources in the core of the older and looser Quintuplet cluster are substantially dimmer and show more diverse spectral characteristics. QX1, with a soft spectrum, is clearly a foreground star, whereas QX4, with a very hard X-ray spectrum, but without a near-IR counterpart, could be either a background AGN or a strongly obscured stellar object. The remaining two (QX2 and QX3) are probably colliding wind binary systems, albeit less energetic than those in the Arches cluster. The Pistol star, despite of its enormous bolometric luminosity, is not detected with a 3σ upper limit to the 0.3-8 keV luminosity as $3{\times}10^{33}$ ergs s^{-1}, consistent with the norminal relation $L_x/L_{bol} \sim 10^{-7}$.

- Diffuse X-ray emission from both Arches and Quintuplet clusters are unambiguously detected. The emission is substantially more extended than the stellar distributions. The emission in the core region of Arches ($r \lesssim 0.6$ pc) has a 2-8 keV luminosity of 4×10^{33} ergs s^{-1}, a steep radial intensity decline, and a hard spectrum with a strong highly-ionized Fe Kα line. These properties are consistent with the cluster wind interpretation.

- The diffuse X-ray emission outside the Arches core, however, has a relatively flat and non-axis-symmetric spatial distribution. The spectrum of the emission shows a distinct 6.4-keV line with an EW of ~ 1.4 keV. This line cannot be explained by the fluorescence of the Arches cluster X-ray emission and is probably due to the collision of low-energy cosmic-ray electrons with neutral or weakly ionized irons in a bow shock, which results from the supersonic motion of the cluster relative to the CS cloud.

- The diffuse X-ray emission from the Quintuplet cluster ($L_X \sim 2 \times 10^{33}$ ergs s^{-1}) is about a factor of 10 lower than from the Arches cluster and can be naturally explained by the cluster wind and a limited number of low-mass pre-main sequence YSOs.

- There appears to be a general deficiency of YSOs in the two clusters, relative to the prediction from the standard Miller & Scalo IMF. Compared with the X-ray emission from young stars in the Orion nebula, our observed total diffuse X-ray luminosities from the Arches and Quintuplet clusters suggest that they contain no more than 2×10^4 and 3×10^3 YSOs. These numbers are a factor of 10 and 5 smaller than what would be expected from the IMF and the massive star popluations observed in the cores of the two clusters. One possibility is that the IMF indeed flattens at intermediate masses, as indicated in a near-IR study of the inner regions of the Arches cluster (Stolte et al. 2005).

- The CS molecular cloud appears to be colliding with the Arches cluster at a relative velocity of $\gtrsim 120$ km s^{-1}, explaining the bow shock morphology of the associated diffuse X-ray emission and its weak correlation with the CS (J = 2–1) line intensity as well as the near-IR extinction distribution and possibly the abnormal kinematics of the dusty gas in the field. Such collisions may be responsible for removing the natal clouds of the clusters at their early ages. High-velocity cloud-cloud collisions might also initiate the formation of massive stellar clusters, such as the Arches and Arches2, with top-heavy IMFs. These are the effects unique in the Galactic nuclear environment.

We thank D. Figer for sending us near-IR data for comparison and for useful discussion on the Arches cluster, A. Stolte for her comments on the MF determination, and the anonymous referee for useful comments and suggestions. This work is supported by NASA through the grant SAO/CXC GO4-5010X.

REFERENCES

Anders, E., & Grevesse, N. 1989, Geochim. Cosmochim. Acta, 53, 197

Baganoff, F. K., et al. 2001, Nature, 413, 45B

Bohlin, R. C., Savage, B. D., & Drake, J. F. 1978, ApJ, 224, 132

Bykov, A. M., Chevalier, R. A., Ellison, D. C., & Uvarov, Y. A. 2000, ApJ, 538, 203

Cotera, A. S., Erickson, E. F., Colgan, S. W. J., Simpson, J. P., Allen, D. A., & Burton, M. G. 1999, ApJ, 461, 750

Cotera, A. S., Colgan, S. W. J., Simpson, J. P., & Rubin, R. H. 2005, ApJ, 622, 333

Cramphorn, C. K., & Sunyaev, R. A. 2002, A&A, 389, 252C

Ebeling, H., White, D. A., & Rangarajan, F. V. N. 2006, MNRAS, submitted (astro-ph/0601306)

Feigelson, E., et al. 2002, ApJ, 574, 258

Feigelson, E. D., et al. 2005, ApJS, 160, 379

Figer, D. F., Mclean, I. S., & Morris M. 1999, ApJ, 514, 202

Figer, D., et al. 1999, ApJ, 525, 750

Figer, D. F., et al. 2002, ApJ, 581, 258

Figer, D. F., Rich, R. M., Kim, S. S., Morris, M., & Serabyn, E. 2004, ApJ, 601, 319

Koyama, K, et al. 1996, PASJ, 48, 249

Gehrels, N. 1986, ApJ, 303, 336

Genzel, R., et al. 2003, ApJ, 594, 812

Hillenbrand, L. A. 1997, AJ, 113, 1733

Kim, S. S., Figer, D. F., Lee, H. M., & Morris, M. 2000, ApJ, 545, 301

Lang, C. et al. 2001a, AJ, 121, 2181

Lang, C., et al. 2001b, ApJL, 551, 143

Lang, C., Goss, W. M., & Morris, M. 2002, AJ, 124, 2677

Lang, C. C., Johnson, K. E., Goss, W. M., & Rodríguez, L. E. 2005, AJ, 130, 2185

Law, C., & Yusef-Zadeh, F. 2004, ApJ, 611, 858

Miller, G. E., & Scalo, J. M. 1979, ApJ, 41, 513

Moretti, A., Campana, S., Lazzati, D., & Tagliaferri, G. 2003, ApJ, 588, 696

Morris, M. 1993, ApJ, 408, 496

Muno, M., Bauer, F. E., Bandyopadhyay, R. M., & Wang, Q. D. 2006, ApJ, in press (astro-ph/0601627)

Nayakshin, S., & Sunyaev, R. 2005, MNRAS, 364, 23

Oskinova, L. M. 2005, MNRAS, 361, 679

Porquet, D., Rodriguez, J., Corbel, S., Goldoni, P., Warwick, R. S., Goldwurm, A., & Decourchelle, A. 2003, A&A, 406, 299

Porquet, D., Grosso, N., Burwitz, V., Andronov, I. L., Aschenbach, B., Predehl, P., & Warwick, R. S. 2005, A&AL, 430, 9

Portegies Zwart S. F., Makino J., McMillan S. L. W., & Hut P., 2002, ApJ, 565, 265

Preibisch, T., Feigelson, & Eric D. 2005, ApJS, 160, 390

Price, S. D., et al. 2001, ApJ, 121, 2819

Raga, A. C., et al. 2001, ApJL, 559, 33

Ramírez, S. V., Sellgren, K., Carr, J. S., Balachandran, S. C., Blum, R., Terndrup, D. M., & Steed, A. 2000, ApJ, 537, 205

Revnivtsev, M. G., et al. 2004, A&A, 425, L49

Rockefeller, G., Fryer, C. L., Melia F., & Wang, Q., D. 2005, ApJ, 623, 171

Schlegel, D. J., Finkbeiner, D. P., & Davis, M. 1998, ApJ, 500, 525

Schild, H., et al. 2004, A&A, 422, 177

Serabyn, E., & Güesten, R. 1987, A&A, 184, 133

Stevens, I. R., & Hartwell, J. M. 2003, MNRAS, 339, 280

Stolte, A., Grebel, E. K., Brandner, W., & Figer, D. F. 2002, A&A, 394, 45

Stolte, A., Brandner, W., Grebel, E. K., Lenzen, R., & Lagrange, A. 2005, ApJL, 628, 113

Sunyaev, R., & Churazov, E. 1998, MNRAS, 297, 1279

Valinia, A., Tatischeff, V., Arnaud, K., Ebisawa, K., & Ramaty, R. 2000, ApJ, 543, 733

van Buren, D., & McCray, R. 1988, ApJL, 329, 93

Wang, Q. D., Gotthelf, E. V., & Lang, C., 2002, Nature, 415, 148

Wang, Q. D. 2003, ANS, 324, 25

Wang, Q. D. 2004, ApJ, 612, 159

Wang, Q. D., Lu, F. J., & Gotthelf, E. V. 2006, MNRAS, 367, 937

Wilms, A., & McCray, R. 2000, ApJ 542, 914

Yusef-Zadeh, F., Morris, M., & Chance, D. 1984, Nature, 310, 557

Yusef-Zadeh, F., et al., 2002, ApJ, 570, 665

Yusef-Zadeh, F., Law, C., & Wardle, M. 2002a, ApJ, 568, 121

Yusef-Zadeh, F., Nord, M., Wardle, M., F., Law, C., Lang, C., & Lazio, T. J. W. 2003, ApJL, 590, 103

Zhekov, S. A., & Skinner, S. L. 2000, ApJ, 538, 808

This 2-column preprint was prepared with the AAS LaTeX macros v5.2.